FRONTIERS OF PHYSICS

TOPICAL REVIEW
Volume 18 / Issue 3 / 33602 / 2023

Optical properties of two-dimensional perovskites

Junchao Hu[1], Xinglin Wen[1,2,†], Dehui Li[1,2,‡]

1 School of Optical and Electronic Information, Huazhong University of Science and Technology, Wuhan 430074, China
2 Wuhan National Laboratory for Optoelectronics, Huazhong University of Science and Technology, Wuhan 430074, China
Corresponding authors. E-mail: †wenxl@hust.edu.cn, ‡dehuili@hust.edu.cn
Received October 12, 2022; accepted December 5, 2022

ABSTRACT

The optical properties of two-dimensional (2D) perovskites recently receive numerous research focus thanks to the strong quantum and dielectric confinement effects. In addition to the strong excitonic effect at room temperature, 2D perovskites also have appealing features that their optical properties can be flexibly tuned by alternating organic or inorganic layers. Particularly, 2D chiral perovskites and 2D perovskites based heterostructures are emerging as new platforms to extend their functionalities. To optimize performance of 2D perovskites-based optoelectronic devices, it is critical to understand the fundamentals and explore the strategies to engineer their optical properties. This review begins with an introduction to the excitons and self-trapped excitons of 2D perovskites. Subsequently, inorganic/organic layer effects on optical properties and 2D perovskites based heterostructures are discussed. We also discussed the nonlinear optical properties of 2D perovskite. We are looking forward to that this review can stimulate more efforts to understand and optimize the optical properties of 2D perovskites.

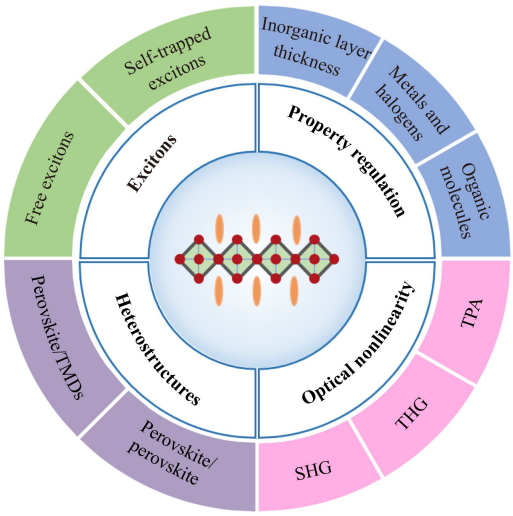

Keywords optical properties, two-dimensional perovskite, heterostructures, self-trapped excitons

Contents

Higher Education Press

https://doi.org/10.1007/s11467-023-1256-8

1 Introduction

Perovskites known as one of the promising optoelectronic materials have attracted intensive attention in the last decade. Until now, broad applications of perovskites in solar cells, photodetectors, light-emitting diodes [1] and lasers have been demonstrated [2–9]. Particularly, the power conversion efficiency (PCE) of three-dimensional (3D) organic–inorganic hybrid perovskite solar cells has been improved to 25.6% due to the excellent light absorbing and charge transporting properties [10]. In addition, perovskites based optoelectronic devices are cheap and easy to fabricate, making it appealing to produce in large scale in industry.

3D halide perovskites have a general formula of ABX_3, where A is monovalent cation [Cs^+, MA^+ ($CH_3NH_3^+$), FA^+ ($CH_2(NH_2)_2^+$)], B is divalent cation (Pb^{2+}, Sn^{2+}, Cd^{2+}) and X is monovalent halide anion (I^-, Br^-, Cl^-). The divalent metal ions and halide interact with each other to form octahedral structure and the monovalent ions are corner-shared by four octahedra. The structure stability can be described by tolerance factor [$t = (R_A + R_X)/2(R_B + R_X)$] proposed by Goldschmidt in 1926 [11], where R_A, R_B and R_X are the radius of cation A^+, metal ions B^{2+} and halide ions X^- respectively. Stable 3D perovskite requires a tolerance factor in the range of $0.8 \leq t \leq 1$. Once A^+ is replaced by larger organic cations, the inter-space between the octahedra is not sufficient to fit the organic cations. Consequently, inorganic layers will be separated to form two-dimensional (2D) perovskites.

In contrast to poor environment stabilities of 3D perovskites, the hydrophobic organic cations in 2D perovskites can serve as a "moisture shielding" layer and thus enhance the ambient stability significantly [9, 12, 13]. Instead of the dominant free carrier effect in 3D perovskites, strong excitonic effect is present at room temperature for 2D counterparts due to the strong quantum and dielectric confinement effects of the quantum well structure [14–16]. In addition, the adjacent layers in 2D perovskites interact with each other by van der Waals force, which makes it feasible to construct heterostructures with other 2D layered materials to realize diverse functionalities. Meanwhile, 2D perovskites also exhibit high light absorption coefficient, moderate charge carrier mobility and appropriate band gap, giving rise to intriguing potential in the applications of environment stable optoelectronic devices.

Although the first 2D layered perovskite was reported by Dolzhenko *et al.* [17] in 1986, they have not received decent attention until recent years. Recently, we have witnessed a rapid development of the research on 2D perovskites. Benefiting from the excellent optical properties, 2D perovskites have been widely studied on solar cells, LED and photodetectors [6, 8, 18–27]. For instance, 2D perovskite solar cell based on $(BA)_2(MA)_2Pb_3I_{10}$ ($BA = C_4H_9NH_3$; $MA = CH_3NH_3$) film was prepared by hot-casting methods with PCE of 12.5% and the encapsulated devices did not show any degradation after 2250 hours light illumination [23]. Moreover, Huang *et al.* [28] reported a multi-quantum well-based LED with external quantum efficiency as high as 11.7%. In addition to solar cells and LED, 2D perovskites were also used in photodetectors. The $(BA)_2(MA)_{n-1}Pb_nI_{3n+1}$ ($n = 1, 2, 3$) 2D perovskites were used to fabricate photodetector with responsivity of 3.00 $mA \cdot W^{-1}$ ($n = 1$), 7.31 $mA \cdot W^{-1}$ ($n = 2$) and 12.78 $mA \cdot W^{-1}$ ($n = 3$) under white light illumination [29].

In addition to the ambient stability, another appealing property of 2D perovskites is that their optical properties can be greatly tailored by controlling the organic cations, metal substitutions, inorganic layer numbers and so on [30–34]. In order to optimize the performance of 2D perovskite optoelectronic devices, it is critical to understand how these factors affect the optical properties. Moreover, 2D chiral perovskites and 2D perovskites based heterostructures are emerging as new research hot spots in the community. In this paper, we will review the optical properties of 2D perovskites with various organic cations, inorganic layers, chiral molecules and van der Waals structures.

Firstly we will introduce the fundamental excitonic properties and self-trapped excitons originated from strong electron–phonon coupling in 2D perovskites. Secondly, we give a systematical overview on optical properties of 2D perovskites with various inorganic layers such as the substitutions of metal and halide ions. Also, change of the inorganic layer number will significantly affect the band structure. Thirdly, the organic cation species and length also have great influence on their optical properties. Particularly, chiral perovskites are formed when chiral molecules are introduced as the organic layer, which show the unique chiral optical properties such as circular dichroism and circularly polarized light emission. Next, novel optical phenomenon of 2D perovskite/2D perovskite and 2D perovskite/transition metal dichalcogenides (TMDs) heterostructures will be introduced. Nonlinear optical properties of 2D perovskites such as second-harmonic generation (SHG), third-harmonic generation (THG) and two-photon absorption (TPA) are discussed as well. Lastly, we summarize the current development and give an outlook regarding the high-performance 2D perovskites optoelectronic devices. We are looking forward to simulating more efforts to understand and optimize the optical properties of 2D perovskites.

2 Excitonic properties

2.1 Excitons in 2D perovskite

2.1.1 Fundamentals

The alternating organic–inorganic layers endow unique

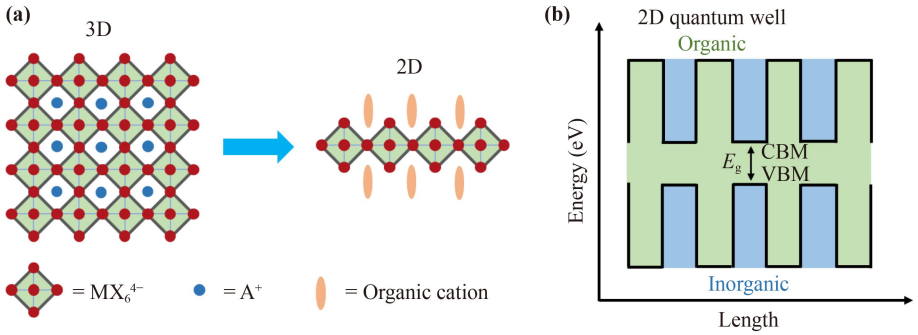

Fig. 1 **(a)** Schematic of 3D and 2D perovskite structure. **(b)** Characteristic band-alignment in 2D perovskites.

quantum well structure of 2D perovskites, which leads to strong quantum and dielectric confinement effects (Fig. 1). The dielectric and quantum confinement effects increase the exciton binding energy significantly compared to 3D perovskites [30, 35, 36]. Charges in 2D perovskites are confined within the inorganic layer due to the organic layer has a higher energy barrier. This quantum confinement effect gives rise to a larger exciton binding energy estimated by $E_b = \left(\frac{2}{\beta-1}\right)^2 E_{b,\,bulk}$ (where β and $E_{b,bulk}$ are dimensionality and exciton binding energy of bulk structure) [37]. When the β is 3 or 2, the $E_b = E_0$ or $4E_0$, respectively. This equation is not suitable for 1D and 0D materials. Consequently, exciton binding energy of 2D perovskites ($\beta = 2$) is almost four times higher than 3D perovskites ($\beta = 3$) [38]. It is noted that the exciton binding energy is also affected by the thickness of inorganic layer. On the other hand, the dielectric constant (ε) of inorganic layers is higher than organic layers and thus give rise to the dielectric confinement effect. The Coulomb interaction between charges in inorganic layer increases as electric field is screened less effectively in adjacent organic layers. The exciton binding energy of 2D perovskites ($n = 1$) is usually around 300 meV and dominant excitonic effects are present at room temperature [30, 38]. Free excitons typically exhibit sharp absorption peak and very narrow photoluminescence (PL) with full-width at half maximum (FWHM) about 20 nm.

The quantum well structure indicates that bandgap of 2D perovskites is mainly determined by the inorganic layer [3, 27]. As a result, the replacement of metal ions, halides and inorganic layer numbers will directly change their bandgap [30, 31, 39, 40]. Besides, the organic layers also have an impact on the optical properties because the organic layers will render inorganic framework tilted and distorted by hydrogen bonding force [41]. For instance, the chiral organic layers can induce optical chirality such as circular dichroism (CD) and circular polarized light emission.

2.1.2 Self-trapped excitons

In addition to narrowband PL of free excitons emission, a broadband PL (FWHM > 100 nm) with large Stokes shift (> 1 eV) can be normally observed in 2D perovskites, which is attributed to the self-trapped exciton (STE) emission. STE is a kind of trapped excitons originated from the strong electron–phonon coupling induced lattice distortion [42–46]. Distinguished from the defect and vacancy states, STE can be produced even in perfect crystals. The threshold of the electron–phonon coupling strength to form STE depends on the dimensionality with the formula of $g_c = 1 - (2v)^{-1}$ (where g_c is the threshold, $v = 6$ and $v = 4$ for 3D and 2D materials). Therefore, STE is easier to be formed in 2D perovskites compared to 3D counterparts. The broadband nature of STE emission is useful in white light generation and thus receive numerous investigations.

The mechanism of the STE origin has been investigated by several research group. By utilizing the transient absorption (TA) spectroscopy [Fig. 2(a)], Zhu *et al.* [45] confirmed that the self-trapped states are indeed caused by electron–phonon coupling and they are enhanced at surface/interfaces where the perovskite crystal structure is most susceptible to deform. Different from the bound states introduced by defects and impurities, the self-trapped states are transient bound states generated by the lattice distortion and they will disappear once the lattice distortion is dismissed. The experiment results also show that STE is more likely to be formed in 2D perovskites compared to 3D perovskites, which agrees with the theoretical prediction as discussed above. In addition, the strength of self-trapped states declines when the inorganic thickness (layer number n) of 2D perovskites increases due to that there are more interfaces with larger n.

Furthermore, Kanatzidis *et al.* [47] investigated the lattice distortion quantitatively by using various bifunctional ammonium such as DMEN (2-(dimethylamino) ethylamine), DMAPA (3-(dimethylamino)-1-propylamine) and DMABA (4-dimethylaminobutylamine). All of (DMEN)$PbBr_4$, (DMAPA)$PbBr_4$ and (DMABA)$PbBr_4$ show a broadband STE emission [Fig. 2(b)]. More importantly, bandwidth of PL is proportional to the octahedral distortion of the inorganic layers. To quantify

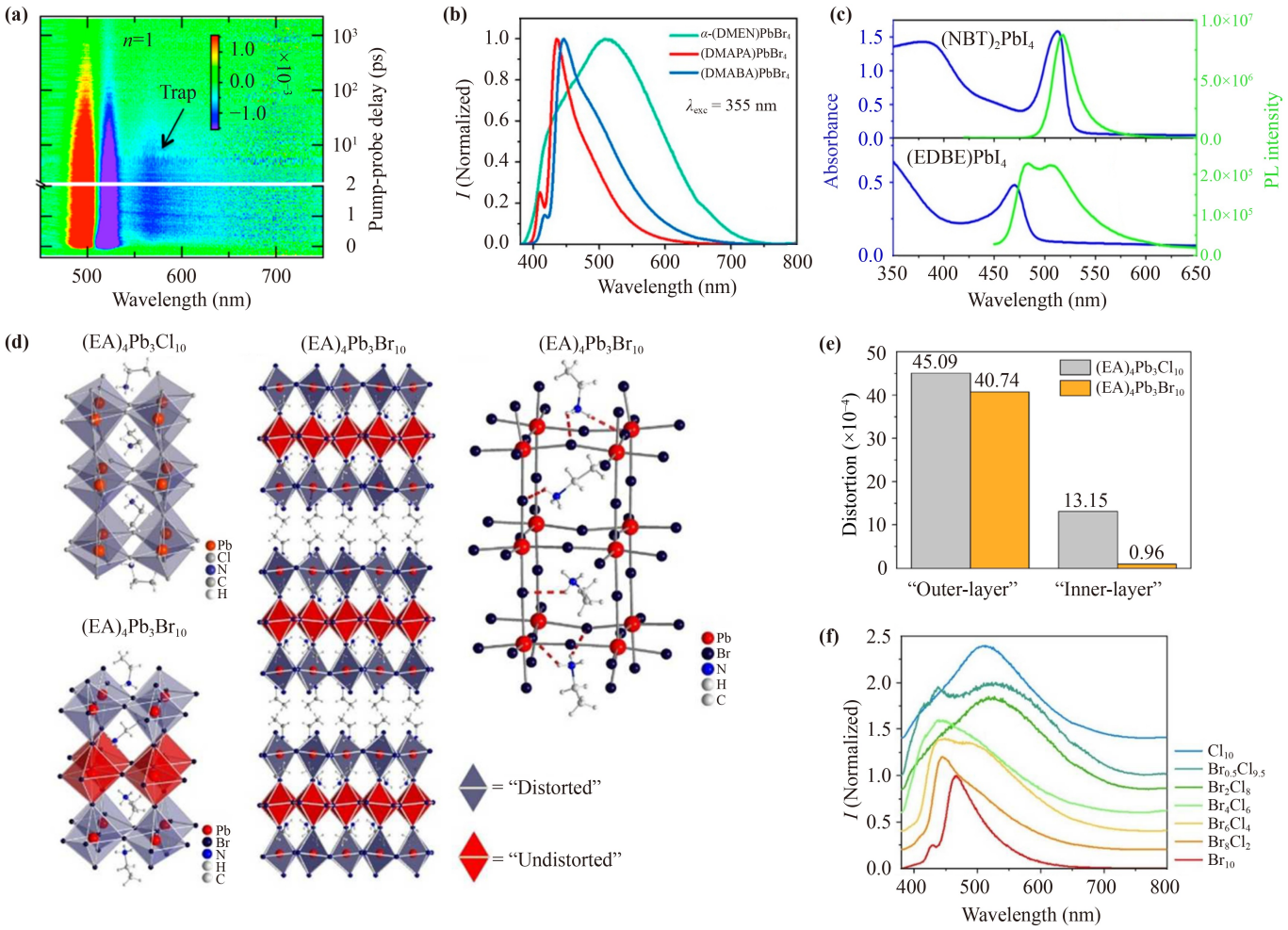

Fig. 2 **(a)** 2D plot of TA spectra of $(BA)_2PbI_4$ film [45]. **(b)** PL spectra of α-(DMEN)$PbBr_4$, (DMAPA)$PbBr_4$ and (DMABA)$PbBr_4$ [47]. **(c)** Absorption and PL of $(NBT)_2PbI_4$ and (EDBE)PbI_4 [43]. **(d)** Structure fragment of three-layered $(EA)_4Pb_3Cl_{10}$, $(EA)_4Pb_3Br_{10}$ and hydrogen bonding network in $(EA)_4Pb_3Br_{10}$. **(e)** Comparison of the distortion level of outer layer and inner layer of $(EA)_4Pb_3Cl_{10}$ and $(EA)_4Pb_3Br_{10}$. **(f)** PL of $(EA)_4Pb_3Br_{10-x}Cl_x$ (x = 0, 2, 4, 6, 8, 9.5 and 10). (d–f) Reproduced from Ref. [48].

the degree of the distortion, the octahedral distortion based on Pb–X bond length is defined as following equation:

$$\Delta d = \frac{1}{6}\sum\left(\frac{d_n - d}{d}\right)^2,$$

where d is the mean distance of Pb-X bond and d_n are the distance of six individual Pb-X bond (X = Br). Experimentally, (DMEN)$PbBr_4$ exhibits broadest exciton emission, which is consistent with that Δd of (DMEN)$PbBr_4$ is largest. The relationship of structure distortion and PL was also studied with $(NBT)_2PbI_4$ and (EDBE)PbI_4 perovskites (NBT = n-butylammonium, EDBE = 2, 2-(ethylenedioxy)bis(ethylammonium)) in Fig. 2(c) [43]. Both the Pb–X length and X–Pb–X angle have impact on the distortion (EDBE)PbI_4 perovskite, leading to larger lattice distortion and a broader PL.

Apart from the organic layer, lattice distortion and STE can also be tailored by engineering the inorganic layer. The structure distortion of $(EA)_4Pb_3Br_{10-x}Cl_x$ perovskite have also been explored by Kanatzidis's group [Figs. 2(d)–(f)] [48]. For three-layered $(EA)_4Pb_3Cl_{10}$ 2D perovskites, outer-layer presents a larger distortion (Δd) than inner-layer up to 45.09 × 10^{-4}. It was also demonstrated that the PL of STE could be regulated by changing the ratio of halide ion of $(EA)_4Pb_3Br_{10-x}Cl_x$. With Cl^- content increasing, the inner-layer PbX_6 octahedra will transit from "undistorted" to "distorted", generating more transient self-trapped states and exhibiting longer PL lifetime.

Because STE emission is closely related to crystal structure, exerting high pressure is an effective method to change structure and optoelectronic properties of 2D perovskites. As reported by Zou's group [49], the $(BA)_4AgBiBr_8$ 2D double perovskites exhibit a broad emission and large Stokes shift under 2.5 GPa pressure,

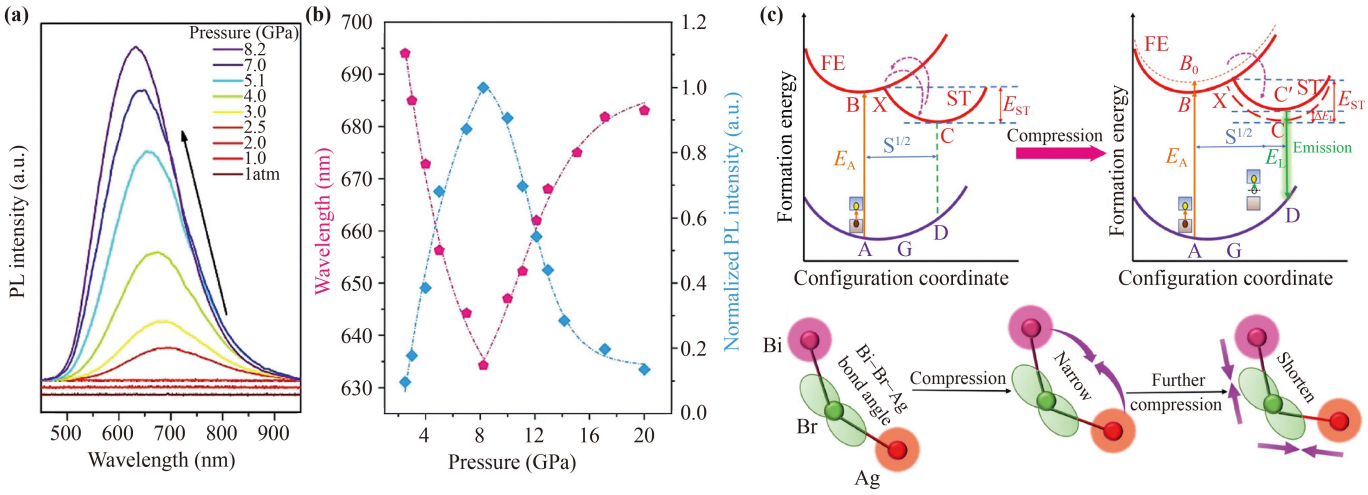

Fig. 3 **(a)** PL spectra of $(BA)_4AgBiBr_8$ under high pressure. **(b)** Pressure dependent PL. **(c)** Mechanism of pressure-induced emission associated with exciton self-trapping at ambient conditions and upon compression. Bi–Br–Ag bond angle is in *bc* plane of $(BA)_4AgBiBr_8$ under compression. Reproduced from Ref. [49].

while it is non-fluorescent initially (Fig. 3). The pressure also make the bandgap narrowed from initial 2.61 to 2.19 eV at 25.0 GPa. They attributed the pressure induced STE to the distortion and compression of the inorganic layer. The inorganic layers undergo two-stages changes. In the first stage, the inorganic Bi–Br–Ag bond angle decreases and the structure distortion is enhanced with increased pressure. While, under a higher pressure condition, the $BiBr_6$ and $AgBr_6$ octahedra shrink to form a new crystalline phase and lead to the luminescence quenching.

2.2 Effect of inorganic layer

2.2.1 Effect of inorganic layer thickness

One of the most appealing features of 2D perovskites is that the bandgap and exciton binding energy can be actively tuned by changing the n value defined as the number of inorganic layers between organic spacer. Because the quantum and dielectric confinement effects become weaker with increased n, the optical properties of 2D perovskites gradually approach to 3D perovskites.

The electronic structure and optical properties of a series of $(BA)_2(MA)_{n-1}Pb_nI_{3n+1}$ and $(BA)_2(MA)_{n-1}Ge_nI_{3n+1}$ (n = 1–5 and $n = \infty$) 2D perovskites are studied by DFT calculations. Both Pb- and Ge-based 2D Ruddlesden–Popper (RP) perovskites share the same trend that the bandgap decreases with n. The bandgap of $(BA)_2(MA)_{n-1}Pb_nI_{3n+1}$ perovskites decreases from 2.37 eV (n = 1) to 1.79 eV (n = 5) and it decreases from 1.92 eV (n = 1) to 1.56 (n = 5) for $(BA)_2(MA)_{n-1}Ge_nI_{3n+1}$ [Figs. 4(a) and (b)] [50]. In addition, the theoretical calculation indicates that the thermodynamic stability of 2D perovskites is notably enhanced than their 3D analogues.

Experimentally, red-shift of exciton absorption and emission can be observed with increased n. For instance, the optical absorption band energy of $(BA)_2(MA)_{n-1}Pb_nI_{3n+1}$ perovskites are 2.43, 2.17, 2.03, 1.91 eV for n = 1, 2, 3, 4 and it finally approach to 1.50 eV for $n = \infty$, namely, the bandgap of 3D $MAPbI_3$ [Fig. 4(d)] [30]. PL red shifts from 2.35 to 1.90 eV when n changes from 1 to 4 [Fig. 4(e)]. In addition, the reduced quantum and dielectric confinement effects render the exciton binding energy decreases when n increases. The exciton binding energy of $(CH_3(CH_2)_5NH_3)_2(CH_3NH_3)_{n-1}Pb_nI_{3n+1}$ declines from 361 meV (n = 1) to 100 meV (n = 4) [51]. Mohite *et al.* [35] developed a generic formulation to determinate the excitons binding energy in low-dimension perovskite system with $E_b = \frac{E_0}{(1+\frac{\alpha-3}{2})^2}$, where $\alpha = 3 - \gamma e^{-\frac{L_W}{2a_0}}$, E_0 is the Rydberg energy, a_0 is Bohr radius of perovskite and L_W is the physical width of the quantum well for an infinite quantum well potential barrier. It predicates that excitons will change to free carrier when the thickness of inorganic layer is larger than 12 nm (n~20).

2.2.2 Metal and halogen atoms substitution

As discussed above, the optical properties of 2D perovskites are primarily determined by the inorganic layers. In 2D perovskites, valence band (VB) consists of hybridization between p orbitals of halogens and s orbitals of metals, while conduction band (CB) is emphatically made of p orbital of metals [30, 50]. For example, VB of the lead iodide-based perovskites consists of hybridized orbitals of I 5p and Pb 6s, while CB is composed of Pb 6p orbitals. Therefore, it is promising to regulate the optoelectronic properties of 2D perovskites by replacing metal or halogen atoms.

$(PEA)_2PbZ_{4(1-x)}Y_{4x}$ (PEA = Phenylethylamine) was

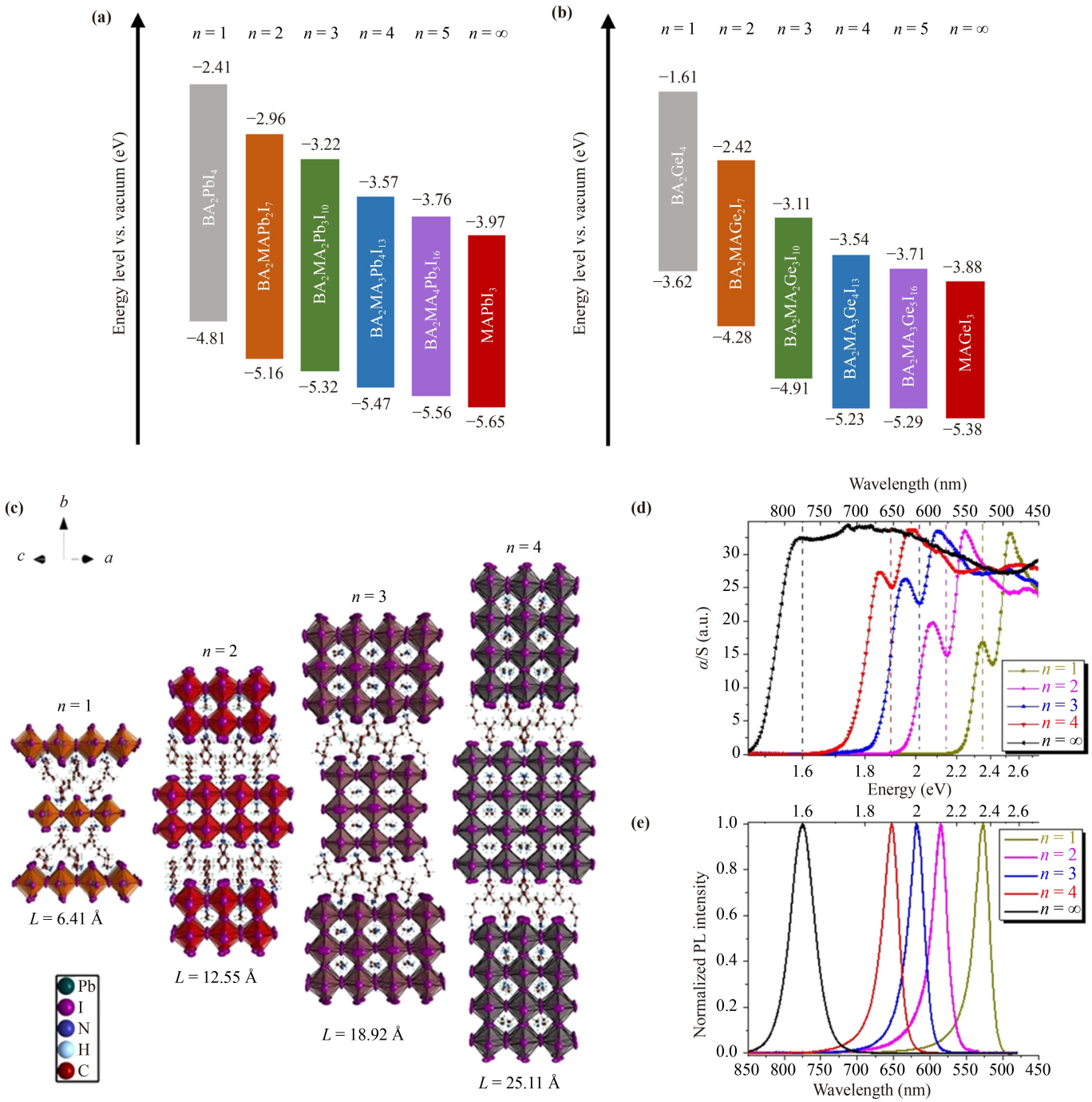

Fig. 4 **(a)** and **(b)** are energy level diagram of 2D RP perovskites $(BA)_2(MA)_{n-1}Pb_nI_{3n+1}$ and $(BA)_2(MA)_{n-1}Ge_nI_{3n+1}$ (n = 1–5 and $n = \infty$) [50]. **(c)** Crystalline structures of the 2D lead iodide perovskites $(BA)_2(MA)_{n-1}Pb_nI_{3n+1}$ (n = 1–4), the L-value denotes the thickness of the inorganic layer in each compound. **(d)** and **(e)** are optical absorption and PL of 2D perovskites with different thickness (n = 1–4 and $n = \infty$). (c–e) Reproduced from Ref. [49].

synthesized by Lauret' group [31], where Z and Y are halogen ions such as I, Br and Cl. The bandgap can be tuned within the range from 3.1 to 3.7 eV by changing the ratio of Br/Cl of $(PEA)_2PbBr_{4(1-x)}Cl_{4x}$ [Figs. 5(a) and (b)]. The absorption of the mixed perovskites comes from the hybridization of the Pb(6s), Z(np) and Y(mp) atomic orbitals. Similarly, Zhang *et al.* [31] synthesized few-layer $(PEA)_2PbX_4$ (X = I, Br, Cl) perovskite nanosheets, and the PL peaks blue shift from 524 nm ($(PEA)_2PbI_4$) to 445 nm ($(PEA)_2PbBr_3I$) with increased Br ratio.

The bandgap of 2D perovskites can also be significantly changed by metal atoms substitution. Theoretical calculations have been employed to obtain the bandgap of 2D

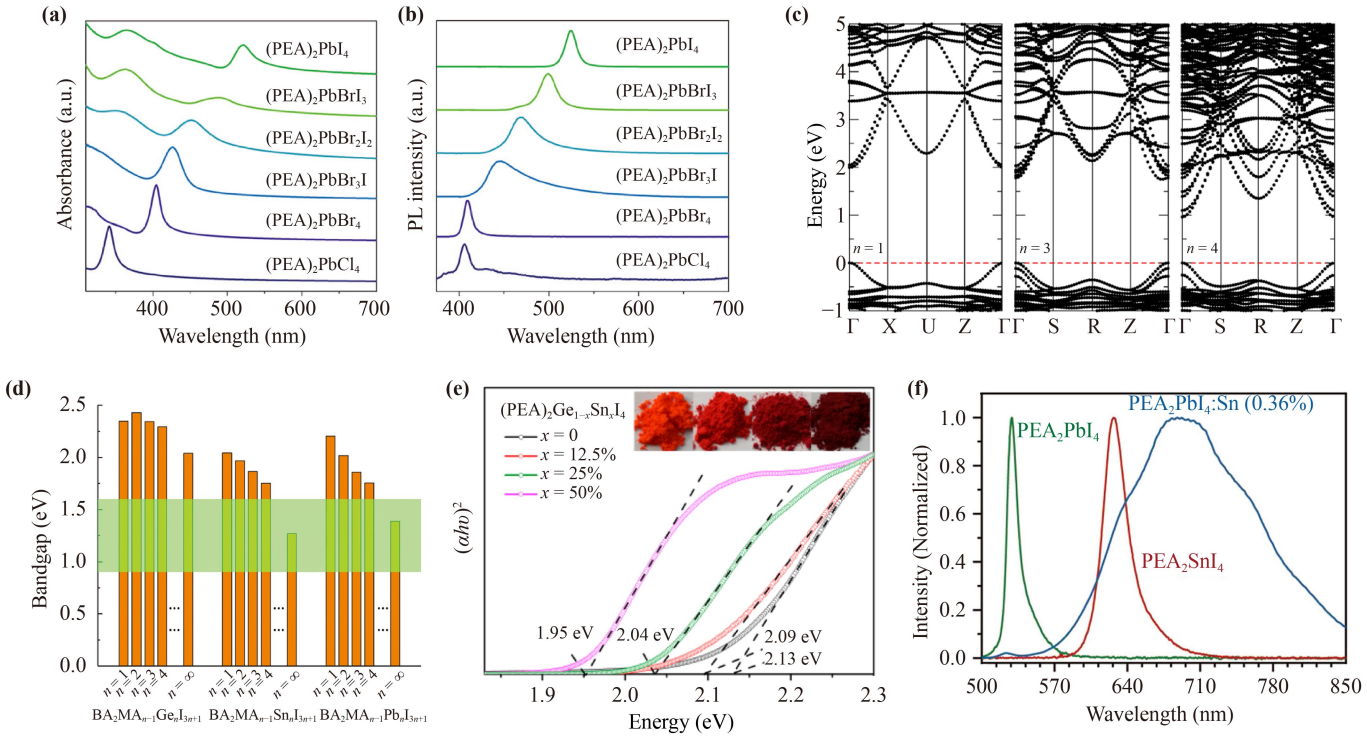

Fig. 5 **(a)** UV-Vis absorption and **(b)** PL spectra of $(PEA)_2PbX_4$ nanosheets (X = Cl, Br, I) with different compositions [31]. **(c)** Electronic band structure of the polar configuration of $(BA)_2(MA)_{n-1}Pb_nI_{3n+1}$ (n = 1, 3, 4) [30]. **(d)** The computed electronic bandgaps of $(BA)_2(MA)_{n-1}M_nI_{3n+1}$ (M = Ge, Sn and Pb; n = 1–4 and $n = \infty$) based on the hybrid functional plus SOC schemes. The light-green horizontal bar denotes the optimal bandgap range (0.9 to 1.6 eV) for solar cells [33]. **(e)** Tauc plots of $(PEA)_2Ge_{1-x}Sn_xI_4$ perovskite with different Sn content [52]. **(f)** PL spectra of bulk crystal of PEA_2PbI_4, PEA_2SnI_4 and PEA_2PbI_4:Sn (0.36%) at room temperature [54].

perovskites with various metal atom substitution [Figs. 5(c) and (d)]. $(BA)_2SnI_4$, $(BA)_2GeI_4$ and $(BA)_2PbI_4$ have the bandgap of 1.45, 1.74 and 1.96 eV, respectively. The coordination symmetry reduction around the cations gives rise to largest MI_6 octahedra distortion of BA_2GeI_4, leading to the lowest bandgap energy. Experimentally, Han *et al.* [52] synthesized a series of 2D mixed Ge–Sn perovskites $(PEA)_2Ge_{1-x}Sn_xI_4$ [Fig. 5(e)] and it was found that the bandgap declined linearly with the increase of Sn contents. The tunable bandgap of Sn-based and Ge-based perovskites offers additional freedom to broaden the operation wavelength range. The Sn incorporation can not only reduce the bandgaps but also improve the moisture stability. Apart from the bandgap engineering, Pb atoms can also be replaced to accomplish lattice distortion. Sn was also introduced by Chen's group [53] to generate broadband red-to-near-infrared-emission at room temperature due to strong exciton-phonon coupling with PEA_2PbI_4:Sn(x) perovskite [Fig. 5(f)], in which Sn dopants initiate the localization of excitons and further induce the lattice distortion around the impurities to obtain STE [54]. In addition, the change of M–X length and M–X–M angle have significant influence on the optical properties. The in-plane and out-of-plane title angle of the inorganic frameworks make the octahedral structure deviate from ideal geometry. The larger title angle will make the orbitals overlapping between metal and halide ions less and less, causing the blue shift of PL [55].

2.3 Effect of organic spacer

2.3.1 Various organic layers

Although the optical bandgap is mainly determined by the components and thickness of inorganic layer 2D perovskites, the organic spacer has nonnegligible influence on the optical properties. Firstly, organic layer as the energy barrier of inorganic layer, the exciton binding energy will be changed by choice of different organic molecules due to their different dielectric constant. Secondly, the chain length of organic spacer will affect the distance between adjacent inorganic layers. Thirdly, the inorganic frameworks interact with organic layer by hydrogen bond, and thus the organic layer will induce distortion inorganic frameworks.

The effect of molecule species and chain length on optical properties of 2D perovskites have been explored. Ishihara *et al.* [38] reported $(C_nH_{2n+1}NH_3)_2PbI_4$ 2D perovskite with different organic chain length (n = 4, 6,

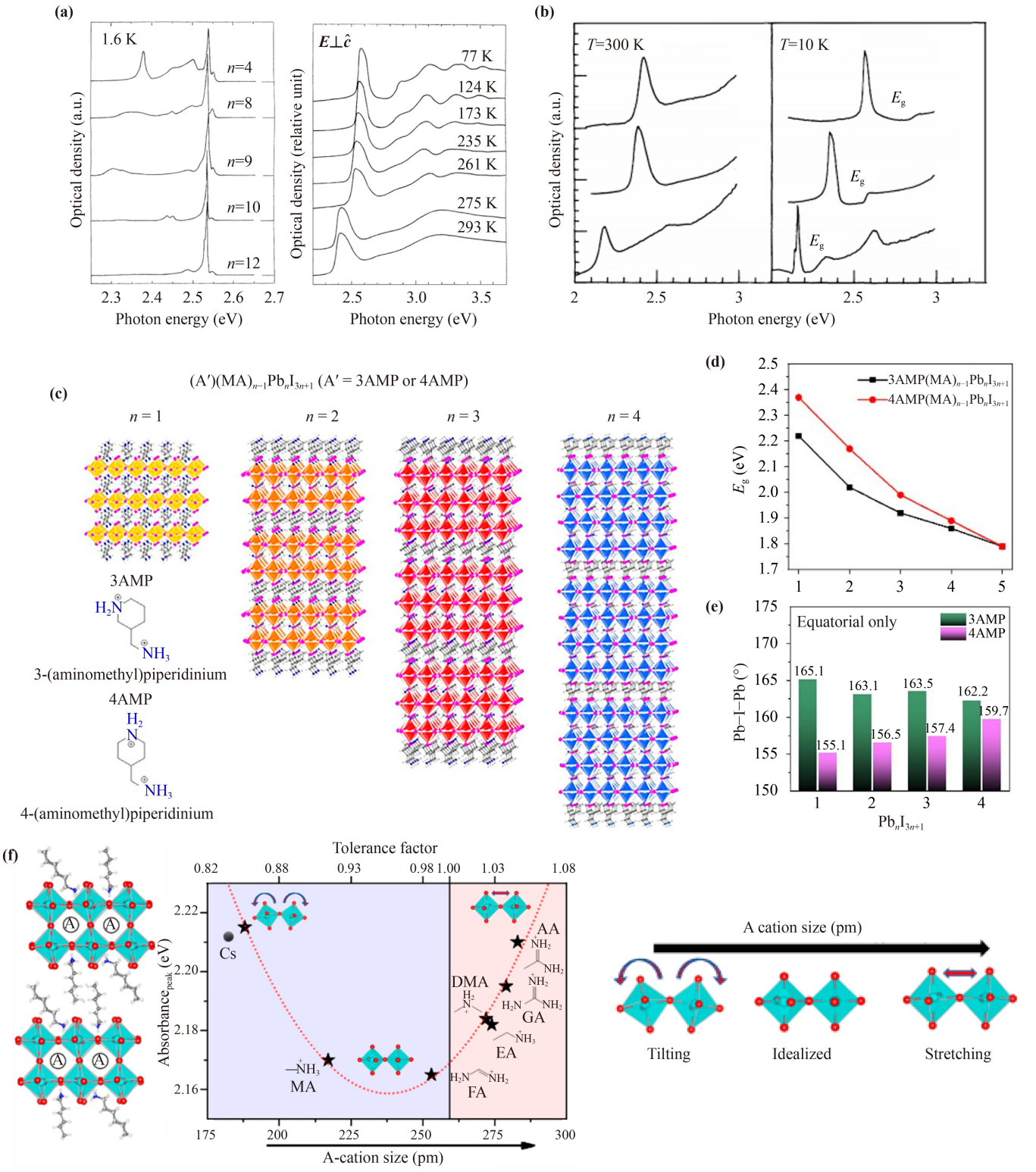

Fig. 6 **(a)** Photoluminescence spectra in single crystal of $(C_nH_{2n+1}NH_3)_2PbI_4$ with $n = 4$, 8, 9, 10 and 12 at 1.6 K and optical density spectra in a cleaved thin crystal of $(C_{10}H_{21}NH_3)_2PbI_4$ at several temperatures [38]. **(b)** Absorption spectra at 300 K and 10 K for $(C_{10}H_{21}NH_3)_2PbI_4$, $(PEA)_2PbI_4$ and $(PEA)_2(MA)Pb_2I_7$ [57]. **(c)** 3-AMP and 4-AMP molecular structure and general crystal structure of the two series of DJ perovskite from $n = 1$ to 4. **(d)** The absorption band energy of $n = 1$ to 5. **(e)** Average equatorial Pb–I–Pb angles for 3-AMP and 4-AMP series from $n = 1$ to 4. (c–e) Reproduced from Ref. [58]. **(f)** Plot of absorbance peak positions verse A-site cation size of $(HA)_2(A)Pb_2I_7$ perovskite, and octahedral structure model of different A cation size [60].

8, 9, 10 and 12) and found the bandgap was no obvious different despite the different spacing [Fig. 6(a)]. Zhang *et al.* [56] reported (F-PEA)$_2$MA$_4$Pb$_5$I$_{16}$ with shorter chain than (PEA)$_2$MA$_4$Pb$_5$I$_{16}$ perovskite and they exhibited enhanced charge transport across adjacent inorganic layers as well as increased carrier lifetime due to the enhanced orbital interactions. Later, dielectric confinement effects of organic layer were explored by Nurmikko's group [Fig. 6(b)]. Although $(C_{10}H_{23}NH_3)_2PbI_4$ and $(PEA)_2PbI_4$ exhibit same bandgap of 2.4 eV, stronger dielectric confinement effect will cause a smaller exciton binding energy. The exciton binding energy are 320, 220 and 170 meV for $(C_{10}H_{23}NH_3)_2PbI_4$, $(PEA)_2PbI_4$ and $(PEA)_2(MA)Pb_2I_7$, respectively [57].

Different from RP phase perovskite with bi-layer organic ligands between Pb-halide octahedral, only a single organic layer in Dion-Jacobson (DJ) phase perovskite will shorten the distance between inorganic layers and reduce the barrier of interlayer charge transport. The influence is ignorable of changing organic molecules in PR phase 2D perovskites; however, optical properties of DJ phase 2D perovskites can be greatly adjusted via choosing asymmetric diammonium cations. The $(A')(MA)_{n-1}Pb_nI_{3n+1}$ DJ perovskites were synthesized by Kanatzidis's group [Fig. 6(c)], where A′ is 3AMP (3-(aminomethyl)piperidinium) or 4AMP ((4-aminomethyl) piperidinium). The 3AMP perovskites show a smaller bandgap than 4AMP perovskite at the same n value [Fig. 6(d)]. The bandgap of 3AMP perovskites are 2.23, 2.02, 1.92 and 1.87 eV for n = 1–4, while the corresponding bandgap of 4AMP are 2.38, 2.17, 1.99, 1.89 eV for n = 1–4 [58]. Analysis on the crystal structure and DFT calculation show the cations cause different optical properties by affecting the Pb–I–Pb angles in equatorial direction. The 3AMP series exhibit a larger Pb–I–Pb angles and induce smaller bandgap than 4AMP [Fig. 6(e)]. Furthermore, DJ phase perovskites with different exciton binding energy were synthesized by choosing BDA (1,4-diammonium) and DMPD (N,N-dimethylpropane diammonium) as organic molecules by Kahn's group [59]. (BDA)PbI$_4$ and (DMPD)PbI$_4$ show exciton binding energy of 390 and 270 meV, respectively. In a word, the small Pb–I–Pb bond angle between lead halide octahedral in the 2D plane is the main reason for larger bandgap and exciton binding energy, which reduces overlap of the Pb 6s and I 5p orbitals.

Beside of organic spacer, the optical bandgap is also influenced by A cation surrounded by octahedral in $n \geq 2$ perovskite. $(BA)_2(FA)_2Pb_3I_{10}$ perovskite film was synthesized by replacing MA with FA and the bandgap (1.51 eV) is much smaller than that of $(BA)_2(MA)_2Pb_3I_{10}$ (2.03 eV) [61]. Recently, a series of 2D $(HA)_2(A)Pb_2I_7$ perovskite nanoplates have been synthesized by Jin's group with different A cations such as Cs, MA (methylammonium), DMA (dimethylammonium) and EA (ethylammonium) to investigate the impact of A cation [60]. As shown in Fig. 6(f), the absorbance of 2D perovskites show the correlation with A cation size. Perovskites with AA (acetamidinium) as A-sites cation have the largest optical bandgap because larger A cation size will generate larger chemical pressure inside the A-site cavity and the Pb-I bond distance increases. In addition, the smaller Cs cation also leads to a larger optical bandgap, which is attributed to the tilted PbI_6 octahedral.

2.3.2 Chiral 2D perovskite

As discussed in last chapter, various organic molecule species are available to serve as the spacer of 2D perovskites. Specially, chiral 2D perovskites are formed when the achiral molecules are replaced by chiral molecules, exhibiting unique chiral optical features except the fundamental optical properties of 2D perovskite. Thanks to the artificial optical chirality, chiral perovskites are of great importance in application of CD, circularly polarized photoluminescence (CPL), circularly polarized detection and spintronics [22, 62–70].

Chiral 1D and 2D perovskites were firstly synthesized in 2003 and 2006, respectively [74, 75]. Chiral functional groups (R- and S-MBA) were introduced as the templating cations and it was found that the crystalline structures depended on the composition of lead halide unites and intermolecular interactions. For instance, face-sharing or corner-sharing 1D chains could be formed for lead chloride and lead bromide, while corner-sharing 2D layers were most likely formed for lead iodide. The optical chirality was firstly reported in 2017 with the demonstration of circularly polarized light absorption (chiroptical activity), which indicates the chirality transfer from chiral organic molecules to achiral inorganic units. Because circularly polarized light carries the information of spin angular momentum and spin-dependent optical selection rule has to be satisfied in optical transitions, chiral perovskites are promising in circularly polarized absorption, detection and emission.

CD, refers to the absorption difference between left-handed and right-handed circularly polarized light, is one of the most prominent features of chiral perovskites. CD is not only used to characterize the chiroptical activity quantitatively, but also utilized to realize the circularly polarized light detection due to the absorption difference [63, 76–78]. Peaks of CD spectra usually occur around the bandgap energy of perovskites because CD response originates from the inorganic sublattice after chirality transfer. The CD properties of 2D chiral perovskite film were studies by Moon's group as shown in Fig. 7(a) [71]. (S-/R-MBA)$_2$PbI$_4$ film exhibit opposite CD peaks at 501, 489, 408 and 367 nm. Whereas, CD signal is absent in the racemic configuration perovskite film. In addition, intensity of CD signal can be adjusted by changing the precursor concentration and coating conditions.

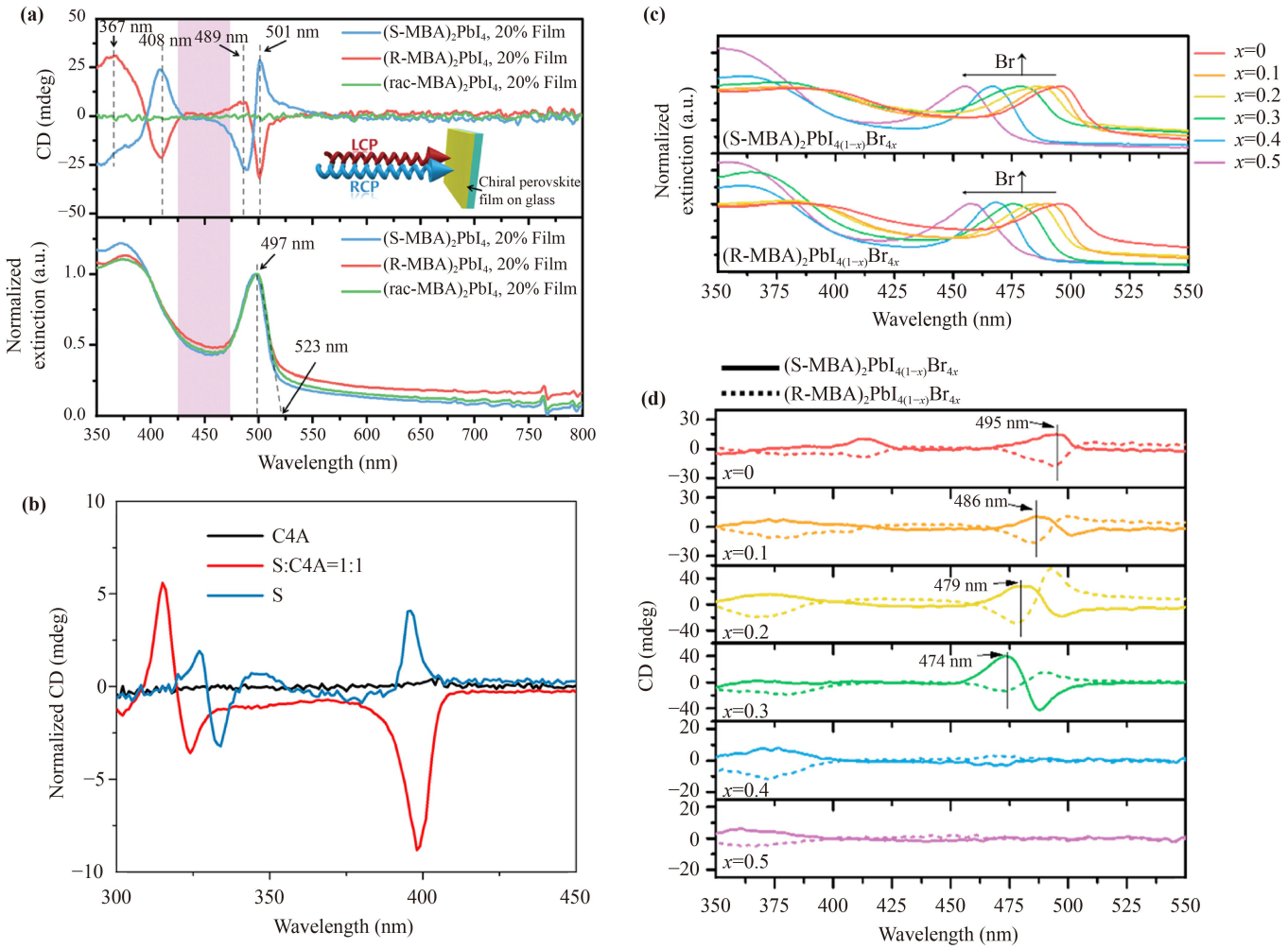

Fig. 7 **(a)** CD spectra and normalized extinction spectra of $(S\text{-MBA})_2PbI_4$, $(R\text{-MBA})_2PbI_4$ and $(rac\text{-MBA})_2PbI_4$ film [71]. **(b)** CD spectra of pure S-MePEA, pure achiral (C4A) and mixed-cation perovskite film [72]. **(c)** Normalized extinction spectra and **(d)** CD spectra of $(S\text{-MBA})_2PbI_{4(1-x)}Br_{4x}$ and $(R\text{-MBA})_2PbI_{4(1-x)}Br_{4x}$ (x = 0, 0.1, 0.2, 0.3, 0.4 and 0.5) film [73].

CD signal can be engineered by changing the chiral spacer cations. The chiral perovskite of mixed cations of chiral aryl molecules and achiral alkyl chain molecule was synthesized by You *et al.* [72], which exhibits a remarkably different CD signal from the purely chiral cation analogues. In addition, the CD signal shows opposite polarity and higher amplitude compared with the corresponding pure chiral perovskite [Fig. 7(b)], which may be related to the spin-splitting in the inorganic layers. Besides, the fact that CD is related to the inorganic sublattice makes it possible to tune CD signals by replacing the lead or halide ions. The mixed halide chiral perovskite $(S\text{-/R-}C_6H_5CH_2(CH_3)NH_3)_2PbI_{4(1-x)}Br_{4x}$ were synthesized by Jooho's group [73]. The CD signal shifts from 495 to 474 nm with increased Br ion contents due to that the bandgap of perovskite is determined by the halide composite-dependent electron energy states [Figs. 7(c) and (d)]. Because the energy of Br 4p orbitals is lower than that of I 5p orbitals in VB, the bandgap can be broadened as Br replace I ions. Furthermore, CD response wavelength range also can be regulated by replacing the metal ions with Sn^{2+}, Cu^{2+}, Bi^{3+}, etc. [68, 79–82].

CPL is another important property of chiral 2D perovskites, which refers to different intensity between the emitted left- and right-handed circularly polarized light under the same excitation condition. CPL stems from the spin-dependent optical selection rule in optical transitions. Sargent *et al.* [70] realized a 3% spin-polarized PL at 2 K in the absence of an external magnetic field [Figs. 8(a)–(c)] [70]. They also found that the chiral response decreased with increased inorganic layer n, which is mainly due to the mole fraction decreasing of chiral molecules. Our group reported a high CPL degree ($P = \frac{I_L - I_R}{I_L + I_R}$) of 17.6% at 77 K with $(S\text{-/R-MBA})_2PbI_4$ chiral perovskite [Figs. 8(d) and 9(e)], where I_L and I_R represent the intensity of the left- and right-handed circularly polarized PL, respectively [83]. The degree of CPL decreases dramatically with increased temperature because thermal vibrations will destroy the helical

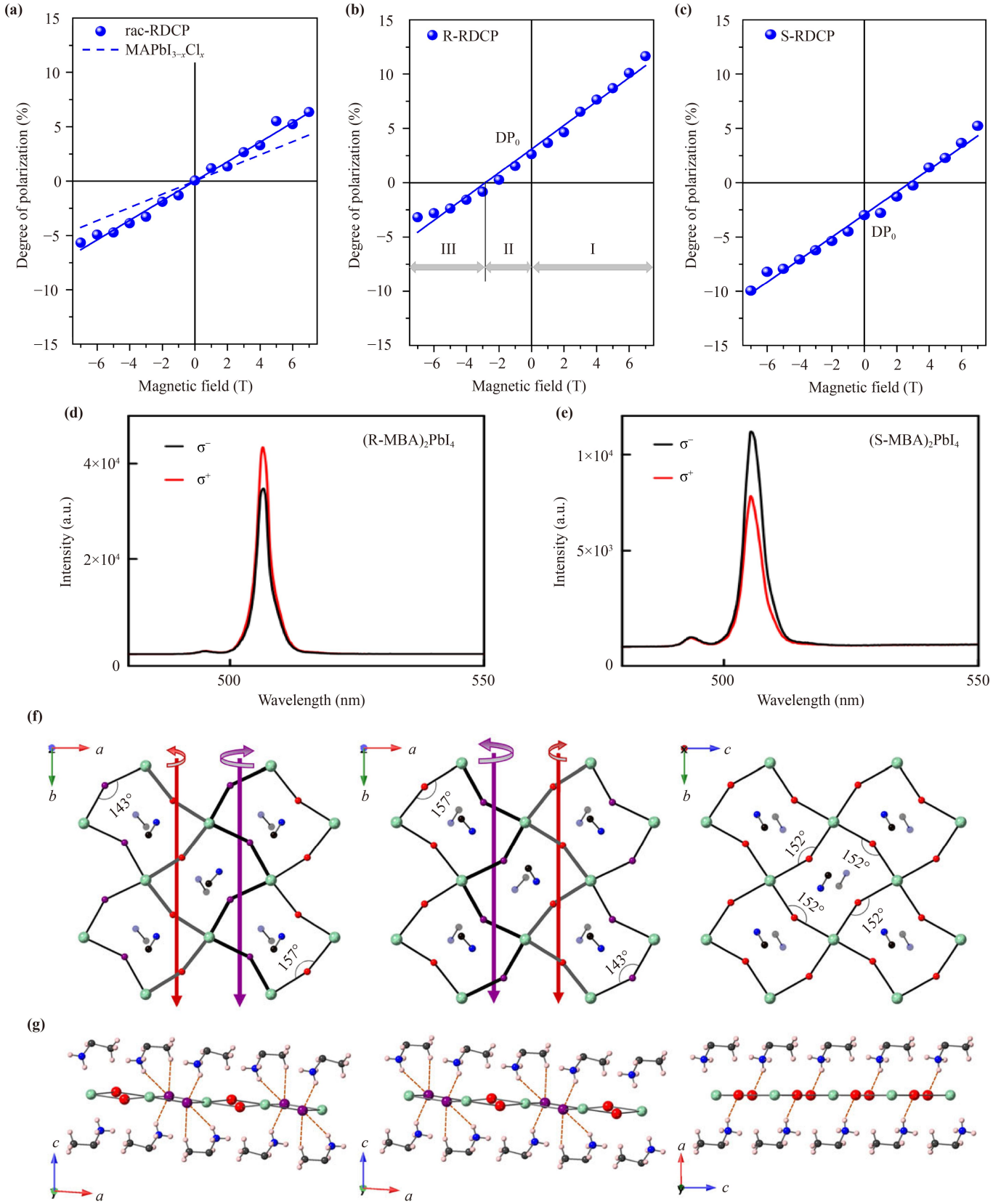

Fig. 8 Degree of polarization for **(a)** racemic-RDCP, **(b)** R-RDCP and **(c)** S-RDCP of low-dimensional perovskites with magnetic field varied from –7 T to 7 T [70]. Circularly polarized PL spectra of **(d)** $(R\text{-}MBA)_2PbI_4$ and **(e)** $(S\text{-}MBA)_2PbI_4$ excited by a 473 nm laser at 77 K [83]. **(f)** In-plane views of $[PbBr_4]^{2-}$ layers in R-NPB, S-NPB and racemic-NPB. **(g)** Hydrogen bonding interactions between the equatorial Br atoms and NEA^+ cations in R-NPB, S-NPB and racemic-NPB [92].

distortion induced chiral molecules. Later, the (S-/R-MBA)$_2$PbI$_4$ chiral perovskites were synthesized by aqueous methods with average CPL degree up to 11.4% and 13.7% for S- and R-hybrids at room temperature respectively [84]. Recently, CPL was achieved in chiral 2D perovskites based LED and it provide a promising strategy to generate circularly polarized light source [85–87]. It is worthy to note that the presence of CD cannot guarantee the observation of CPL. CPL is closely related to the radiative and nonradiative recombination kinetics and large CPL degree can be expected only if excitons recombine radiatively prior to spin flipping.

Revealing the mechanism of optical chirality generation is essential for device design and performance optimization. Up to now, four different chiral mechanisms have been proposed to explain chirality generation, which includes: i) chiral structure induced by chiral molecules; ii) electronic interactions between the chiral ligands and inorganic frameworks; iii) chiral surface distortions induced by chiral organic layer; iv) surface enantiomeric chiral distortions [83, 88–91].

Although the mechanism is still in debate, most reports tend to indicate that the structure change induced by chiral molecules incorporation is primarily responsible to the emergence of chirality [22, 69, 71, 83]. Different from the centrosymmetric structure of achiral perovskites, the chiral organic layers render the inorganic octahedral layer title and break the inversion symmetry. Consequently, chirality can transfer from chiral molecules to inorganic layers. It was reported that R- and S-NPB (NPB = 1-(1-naphthyl)ethylammonium) chiral spacer cations exhibited asymmetric hydrogen bonding interaction with $[PbBr_4]^{2-}$ layers, causing out-of-plane helical distortions in the inorganic layers with Pb–Br–Pb angles of 143° and 157° respectively [Figs. 8(f) and (g)] [70, 92]. However, the racemic-NPB achiral spacer does not show out-of-plane helical distortions in the inorganic layers with Pb–Br–Pb angles of 152°. First principles calculations indicate that the combination of out-of-plane helical distortion and strong spin-orbit coupling in $[PbBr_4]^{2-}$ layers give rise to the Rashba-Dresselhaus spin-splitting in conduction band with opposite spin textures between R- and S-NPB. It is the opposite spin textures that cause the chiroptical activities of chiral 2D perovskites. Furthermore, the chiral transfer depth was also explored by Luther's group [93], the S-MBA molecular transfers chirality to perovskite nanocrystals by structure distortion. The theoretical simulations show that the interface layer have a maximum in-plane Pb–Br–Pb angle distortion, and the effextive depth of monolayer chiral molecule is up to five outermost layers of surface octahedral. It also indicated that the chirality is gradually decreasing with increasing n value. In addition, the distortion index (D) and bond angle variance (σ^2) were used to quantify the degree of octahedral distortion: $D = \frac{1}{6}\sum\left|\frac{d_i - d_0}{d_0}\right|$, $\sigma^2 = \frac{1}{11}\sum(\theta_i - 90)^2$, where d_i represents the individual Pb–X bond lengths, d_0 is the mean Pb–X bond angle, θ_i is the octahedral X–Pb–X bond angles. The D and σ^2 should be exactly 0 in an ideal octahedron [68]. The chiral perovskite shows a larger distortion index than achiral perovskite due to chiral molecules induced structure distortion.

Moreover, the generacy of energy states is broken in chiral perovskite and, the total angular moment quantum number j remains same. However, the magnetic quantum number m_s are different, which makes the spin down energy state $|j,-\frac{1}{2}\rangle$ is different to the spin up energy state $|j,+\frac{1}{2}\rangle$ [66, 73]. Thus, the spin-polarized carriers can be generated with circularly polarized light excitation.

Electronic interactions have a significant influence to chiro-optical response of chiral perovskite. Figure 9(a) shows that the CD signal are related with the concentration and temperature of the R-/S-PEA perovskite nanoplate solution [94]. The chiroptical response is generated from quantum-confined perovskite electronic states of chiral ligands, and affected by chiral ligand arrangement on the perovskite surface as well.

The chirality was also affected by surface distortions induced by chiral organic layer. Zhang *et al.* [89] used 1-, 2-diaminocyclohexane (DACH) as chiral molecular to induce chiroptical activity in $CsPbBr_3$ nanocrystal [Fig. 9(b)]. The chiroptical properties of $CsPbBr_3$ nanocrystal strongly on the amount of chiral ligands, indicating the chiral surface distortion and electronic interactions between DACH and perovskite are the main reason to chirality origin [89]. Furthermore, the effect of chiral ligand ratio on chirality of 2D perovskite also studied by Waldeck's group. The chiral signal of (R-/S-PEA)$_2$ $MAPb_2I_7$ nanoflakes are strong depends on the ratio of chiral molecular [Fig. 9(c)]. In addition, a chirality saturation phenomenon occurs, which is related to the size of ligand molecular [90].

Beside, the chirality also could be achieved by stacking a liquid crystal (LC) cholesteric superstructure on the perovskite surface [Fig. 9(d)], in which the LC was used as filter and convert unpolarized light to circular polarized light [91]. A 100% circular polarization conversion efficiency could be achieve by selective reflection of the LC film. The CPL could be modulated by shifting the overlap of reflection band and the emission band.

In all of the proposed mechanisms, the chiral molecular induce structure distortion have been accepted as one of the main mechanisms of chiral origin of chiral perovskite by most of researchers, considering the chiral molecular layer is the only chiral source to induce distortion of inorganic frameworks in pure chiral perovskite. However, there need more exploration to completely understand the chirality origin of chiral perovskites.

2.4 2D perovskites based heterostructure

2.4.1 2D perovskite/2D perovskite

Similar to TMDs, the van der Waals (vdW) interaction

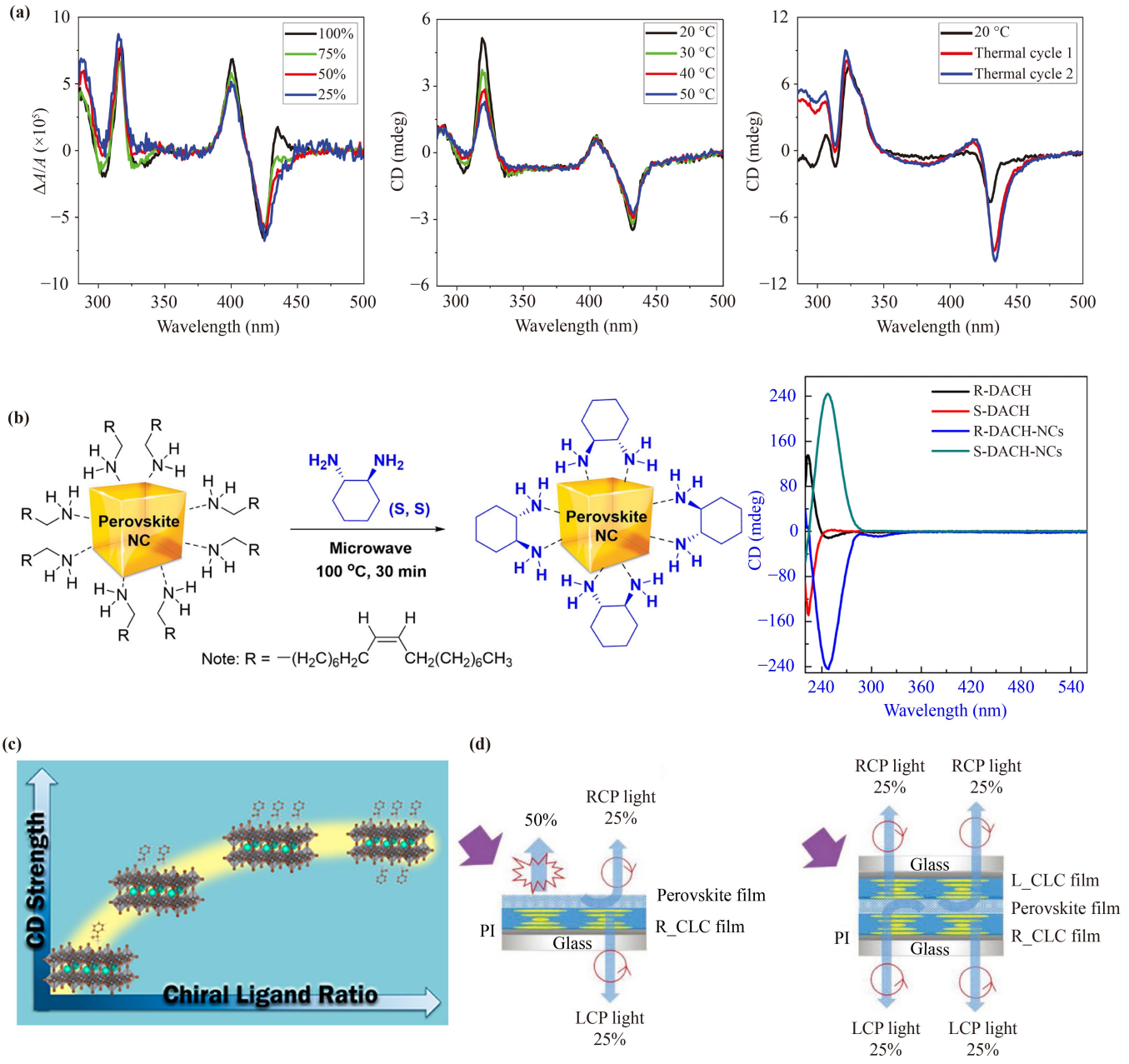

Fig. 9 **(a)** Dependence of the circular dichroism (CD) signal on the concentration and temperature of the nanoplatelet (NP) solution [94]. **(b)** Ligand exchange on an OA-capped perovskite NC using pure enantiomers of DACH and CD spectra of low concentrations of DACH [89]. **(c)** Schematic representation of CD ligand ratio and CD strength of chiral perovskite nanoplates [90]. **(d)** Working principle of the circularly polarized light (CPL) system with the handedness superstructure stack [91].

between adjacent layers of 2D perovskites gives rise to the flexibility of integrating with various layered materials to build heterostructures, which is an appealing feature of 2D perovskites compared to 3D counterparts. Formation of heterostructures not only offers the opportunities to study the physics of energy and charge transfer, but also can enrich optical properties to broaden their applications. Up to now, various 2D perovskites based heterostructures have been demonstrated including 2D perovskite/2D perovskite, 2D perovskite/TMDs, 2D perovskite/graphene and 2D perovskite/black phosphorous heterostructures [95–105].

The chemical synthesis and mechanical exfoliation are the main methods to fabricate perovskites heterostructures. Normally, chemical synthesis methods are usually used for perovskite-perovskite heterostructure fabrication. Chemically synthesized heterostructures exhibit strong interlayer coupling and efficient carriers transfer

can be attained at the interface. Nonetheless, successful synthesis can be only achieved for some specific materials and the synthesis condition is critical as well. The $(PEA)_2PbI_4/(PEA)_2(MA)Pb_2I_7$ vertical heterostructure was firstly synthesized by a solution growth method [97]. The type I band alignment makes the internal energy transfer from $(PEA)_2PbI_4$ layer to $(PEA)_2(MA)Pb_2I_7$ under the time scale of hundreds of picoseconds [Figs. 10(a) and (b)]. Our group also successfully synthesized $(BA)_2PbI_4/(BA)_2(MA)Pb_2I_7$ vertical heterostructure with a solution synthesis method by making use of the different solubility of $n = 1$ and $n = 2$ crystals [Fig. 10(c)] [96]. The thickness and junction depth can be controlled by controlling concentration, temperature and reaction time. Photodetector based on such heterostructure exhibit dual-band spectral response with a full-width at half-maximum of 20 nm at 540 nm and 34 nm at 610 nm. This synthesis strategy is also applicable to synthesize other perovskite heterostructures, and the band alignments of heterostructures can be tailored by changing metal and halide components.

Alignment transfer of the mechanical exfoliated flakes is another typical method to fabricate heterostructures, in which the atomic thin layer with thickness down to monolayer can be obtained. Moreover, the stacking material, order, thickness and angles are adjustable, offering more flexibility to optimize the optical response of heterostructures. The highly quality exfoliated vertical perovskite heterostructures $(BA)_2PbBr_4/(BA)_2(MA)_2Pb_3I_{10}$ were reported at 2021 by Dou' group [99]. Apart from the charge transfer, they found the $(BA)_2PbBr_{4x}I_{4(1-x)}$ alloy were formed at the interface due to I^- ions diffusion from $n = 3$ to $n = 1$ layer, which exhibited a new PL peak around 512 nm [Figs. 10(f) and (g)]. The ion diffusion also could be observed in other 2D perovskite heterostructures and it provide a new insight for studies of complex superlattices and devices. Unlike the vertical heterostructures, the lateral heterostructures are more difficult to fabricate and it can be only prepared by chemical synthesis methods

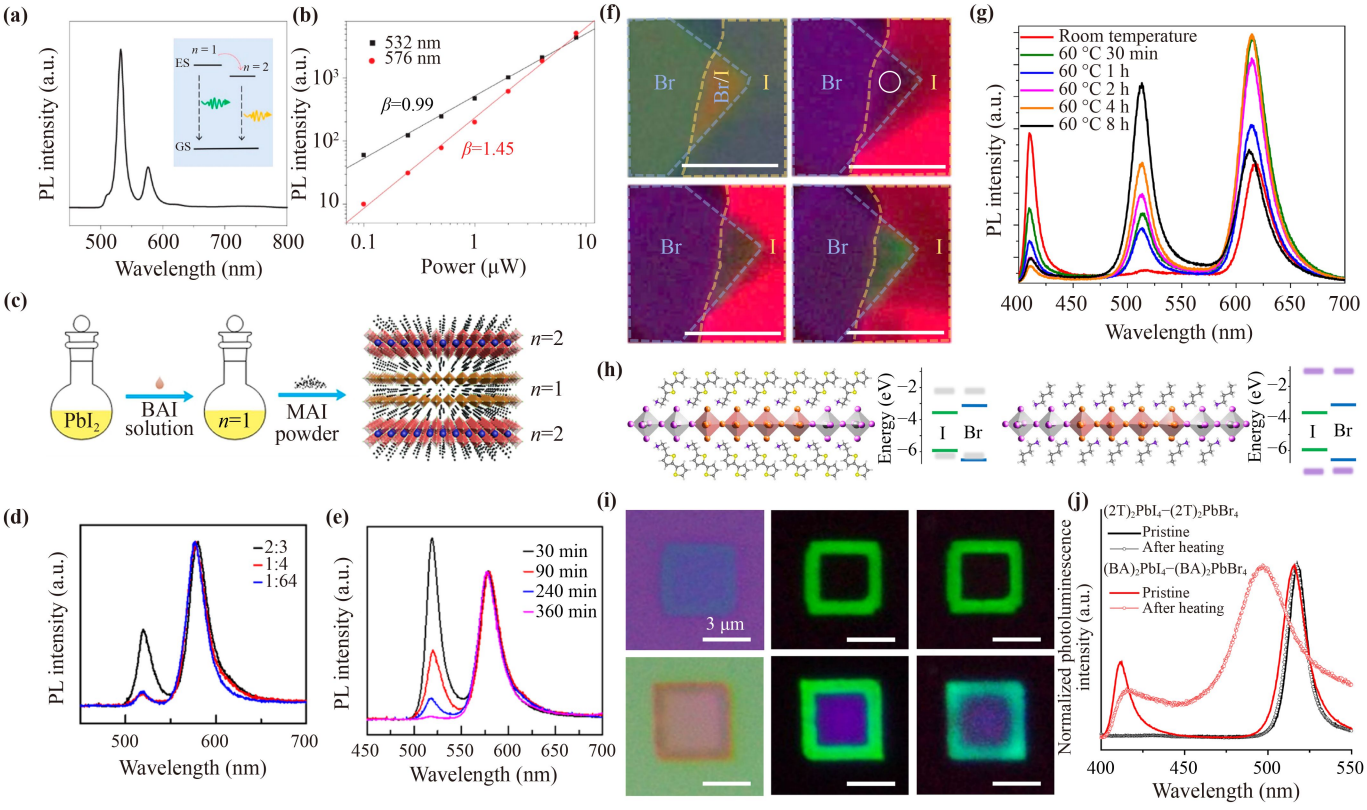

Fig. 10 **(a)** PL of $(PEA)_2PbI_4/(PEA)_2(MA)Pb_2I_7$ 2D perovskite heterostructures. **(b)** PL of the 532 nm ($n = 1$) and 576 nm ($n = 2$) peaks as a function of excitation power. The β indicates the slope of the relation. (a, b) Reproduced from Ref. [97]. **(c)** Schematic illustration of the synthesis of $(BA)_2PbI_4/(BA)_2(MA)Pb_2I_7$ heterostructures. **(d)** Normalized PL of $(BA)_2PbI_4/(BA)_2(MA)Pb_2I_7$ heterostructures with different mass ratios of BAI/MAI. **(e)** Normalized PL of $(BA)_2PbI_4/(BA)_2(MA)Pb_2I_7$ heterostructures with different maintaining times for a fixed MAI concentration. (c–e) Reproduced from Ref. [96]. **(f)** PL images of the vertical heterostructures $(BA)_2PbBr_4$-$(BA)_2(MA)_2Pb_3I_{10}$ under the heating treatment process. **(g)** Evolution of PL of the vertical heterostructures upon heating at 60 °C. (f, g) Reproduced from Ref. [99]. **(h)** Schematic illustrations and proposed band alignments of $(2T)_2PbI_4$-$(2T)_2PbBr_4$ and $(BA)_2PbI_4$-$(BA)_2PbBr_4$ lateral heterostructures. **(i)** Optical and PL images of lateral heterostructures. **(j)** PL of the heterostructures before and after heating. (h–j) Reproduced from Ref. [98].

under specific condition. Dou *et al.* [98] reported a highly stable and tunable lateral heterostructures, multi-heterostructures and superlattices by epitaxial growth, such as $(PEA)_2PbI_4$–$(PEA)_2PbBr_4$ and $(4Tm)_2SnI_4$–$(4Tm)_2PbI_4$ heterostructures. The band alignments can be engineered either by changing the inorganic composite in the lateral in-plane direction or by modifying the molecular structure in the out-of-plane direction [Figs. 10(h)–(j)]. The ion diffusion across 2D halide perovskite heterostructure can be substantially inhibited by using rigid conjugated ligands and near-atomically sharp interfaces could be obtained.

2.4.2 2D perovskite/TMDs

The optical properties of TMDs vdW heterostructures have been widely studied and interlayer excitons (IXs) can be formed with electrons and holes residing in different layers [106–110]. The spatial separation of electrons and holes renders long lifetime of IXs, which is favorable for applications in valleytronics and optoelectronics. Nevertheless, the properties of IXs in TMDs heterostructures highly depend on the twist angle between two layers and thermal annealing is usually necessary to enhance the interlayer interaction [110]. Heterostructures made of 2D perovskites and TMDs provide a new platform for IXs. The strong interlayer coupling can be robustly achieved in 2D perovskites/TMDs heterostructures without considering twist angle and thermal annealing, which greatly simplify the fabrication process and makes it more suitable for practical applications [104, 111, 112].

Our group reported that IXs could be robustly formed in 2D perovskites/monolayer TMDs regardless of stacking order [100, 101, 105, 112]. IXs exhibit a broadband emission and blue-shifted PL with the increased excitation power due to the dipole-dipole interaction. In addition, our group reported the IXs can be tuned in large spectra range by changing layer numbers of TMDs [105]. Because it transits from direct to indirect bandgap when TMDs change from monolayer to multilayers, momentum-indirect IXs are observed in 2D perovskites/few-layer TMDs heterostructures [Figs. 11(a)–(c)]. The emission energy of IXs could be tuned from 1.3 to 1.6 eV by changing the WSe_2 layers and the n value of $(iso\text{-}BA)_2(MA)_{n-1}Pb_nI_{3n+1}$ from 1 to 4. IXs in those heterostructures also show a large diffusion coefficient of 10 $cm^2 \cdot s^{-1}$.

Apart from the charge transfer and IXs formation, it was also reported monolayer WS_2/PEA_2PbI_4 heterostructure exhibited the Förster type energy transfer from perovskite to WS_2 [Figs. 11(d) and (e)] and PL enhancement could be observed with enhancement factor up to 8 [104]. The analysis concluded that energy transfer not only occur at the interface between WS_2 and PEA_2PbI_4, energy transfer across the inner layers of 2D perovskites also contributed to the PL enhancement.

Due to the capability of controlling spin with chiral 2D perovskite, chiral perovskite based heterostructures are promising to achieve spin injection [Figs. 11(f)–(h)]. Selective spin injection in $(S\text{-}MBA)_2PbI_4/WSe_2$ and $(R\text{-}MBA)_2PbI_4/WSe_2$ was demonstrated with impressive average spin injection efficiency of 78% [100]. The spin injection could produce persistent valley polarization in monolayer MoS_2 or WSe_2 over 10%, which suggests chiral 2D perovskites are of great importance to manipulate the valley degree of freedom of TMDs [101]. Different from the conventional spin injection with electric filed driven ferromagnets, chiral 2D perovskites based spin injection provides advantages of external field free, simplified device structure and smaller device size. We believe chiral 2D perovskites/TMDs heterostructure can play an important role in valleytronics.

Beside the chiral 2D perovskites/TMDs heterostructure, the spin electron injection also occurs inside chiral perovskite/achiral perovskite heterostructure. Recently, $(R\text{-}/S\text{-}MBA)_2PbI_4/(PEA)_2(MA)Pb_2I_7$ heterostructures have been fabricated by Wang's group [113]. The CPL could be observed in achiral perovskite by receiving spin-polarized electrons form chiral perovskite with CPL degree of 13.8% at 80 K under 532 nm laser excitation. It provides a new pathway to endow CPL activity for achiral perovskites.

3 Nonlinear optical properties of 2D perovskite

In addition to the linear optical properties as discussed above, nonlinear optics (NLO) of 2D perovskites attract numerous attention as well. NLO refers to the nonlinear response when matters interact with intense light, in which the induced polarization is nonlinearly dependent on the incident electric field and can be expressed as the following formula:

$$P = \varepsilon_0 \left(\chi E + \chi^{(2)} E^2 + \chi^{(3)} E^3 + \cdot\right) = \varepsilon_0 \chi E + P_{\mathrm{NL}},$$

where ε_0 is the vacuum permittivity, $\chi^{(n)}$ is the nth-order optical susceptibility [114–119]. It can be seen that the induced polarization mainly consists of two parts: linear polarization of $\varepsilon_0 \chi E$ and nonlinear polarization of P_{NL}. For a moderate incident light field, only linear terms can be observed, such as linear absorption and refraction. However, the nonlinear term cannot be negligible under strong excitation. Second- and third-order nonlinearity are mainly reported for 2D perovskites such as second harmonic generation (SHG), third-harmonic generation (THG) and two-photon absorption (TPA).

3.1 Second-harmonic generation

Second-order nonlinearity is normally vanished in 2D perovskites due to their centrosymmetric structure.

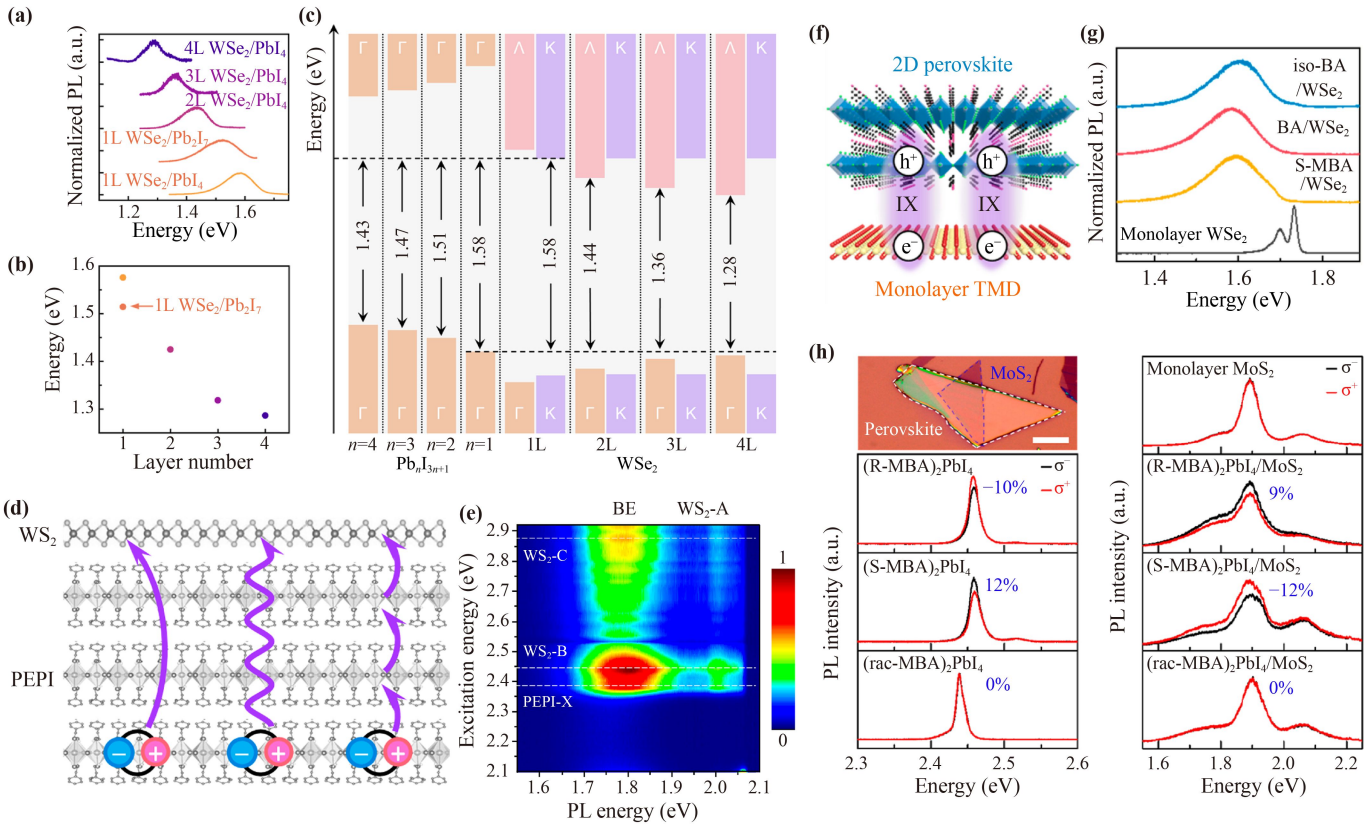

Fig. 11 **(a)** Normalized PL of $WSe_2/(iso\text{-}BA)_2PbI_4$ ($x = 1, 2, 3, 4$) and 1L $WSe_2/(iso\text{-}BA)_2(MA)Pb_2I_7$ vdW heterostructure. **(b)** IXs emission energy as a function of the layer number x of the constituent materials and **(c)** band alignment of the vdW heterostructure formed by WSe_2 and $(iso\text{-}BA)_2(MA)_{n-1}Pb_nI_{3n+1}$ perovskites. (a–c) Reproduced from Ref. [105]. **(d)** Different electron transfer routes for excitons generated far from the $WS_2/(PEA)_2PbI_4$ interface. **(e)** PLE of a heterostructure at 110 K. (d, e) Reproduced from Ref. [104]. **(f)** IXs in the 2D perovskite/monolayer TMD heterostructure. **(g)** IXs emission of $(iso\text{-}BA)_2PbI_4/WSe_2$, $(BA)_2PbI_4/WSe_2$ and $(S\text{-}MBA)_2PbI_4/WSe_2$ under a 633 nm laser excitation. (f, g) Reproduced from Ref. [100]. **(h)** Manipulation of valley polarization in monolayer MoS_2 via chiral 2D perovskite/MoS_2 heterostructure [101].

Recently, chiral spacer cations have been introduced to break the inversion symmetry and consequently induce SHG. Xu *et al.* [120] fabricated a non-centrosymmetric 2D perovskite nanowires $(S\text{-/R-MPEA})_{1.5}PbBr_{3.5}(DMSO)_{0.5}$ by using chiral amines as the organic component. Dimethyl sulfoxide (DMSO) molecules axially coordinate with Pb^{2+} in the partially edge-shared octahedrons, which results in the structural symmetry breaking of this 2D perovskite [Figs. 12(a)–(c)]. Under the pump of 850 nm linearly polarized fs pulsed laser, the nanowires exhibited an effective second-order NLO coefficient of 0.68 pm·V^{-1} and a linear polarization ratio of $(96.4 \pm 0.1)\%$. Moreover, the SHG-CD was up to $(74.0 \pm 0.1)\%$ when pumped with circularly polarized light. Wu *et al.* [121] prepared $(S\text{-/R-ClPEA})_2PbI_4$ 2D perovskite microwire array (ClPEA = 1-(4-chlorophenyl)ethylamine) which shown linearly polarized SHG and two-photo fluorescence [Figs. 12(d)–(f)]. Under the pump of linearly polarized fs laser pulse at 800 nm, the maximum SHG intensity was observed when the polarization was parallel to the axial of the microwires. Anisotropic SHG ratio of 23.2 and 21.3 were observed in $(S\text{-/R-ClPEA})_2PbI_4$, respectively.

Recently, the chiral lead-free double perovskite microwire arrays of $(S\text{-/R-3AP})_4AgBiBr_{12}$ for anisotropic SHG have been reported by Wu's group [Figs. 12(g)–(i)], which was synthesized by capillary-bridge confined assembly technique [122]. The linear polarized SHG anisotropy of microwires is up to 0.92 with the nonlinear coefficient of 0.28 pm·V^{-1} under 800 nm excitation.

The influence of organic layer on SHG anisotropy was also discussed by Lu *et al.* [123]. The in-plane SHG anisotropy of 2D perovskite $(C_6H_5CH_2NH_3)_2PbCl_4$ decreases with the thickness decreasing of perovskite nanoflakes. The theoretical calculation results show that the conformational of organic amine cations alternates with the reduced thickness due to weakened van der Waals interactions, leading to the changes in orientation of electric dipoles and corresponding SHG anisotropy.

3.2 Third-harmonic generation

In contrast to SHG, the non-centrosymmetric structure

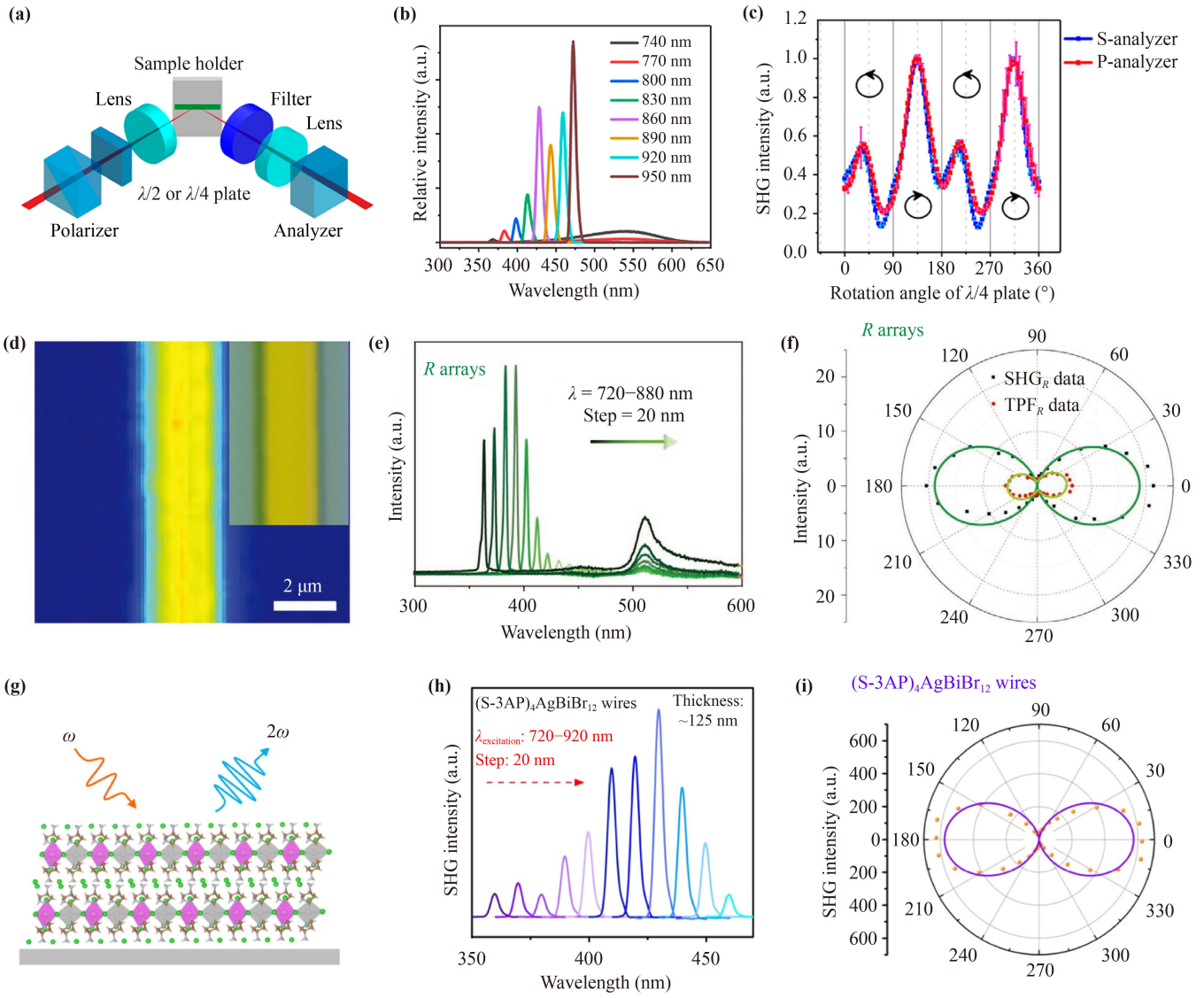

Fig. 12 **(a)** Schematics of the SHG measurements. $\lambda/2$ and $\lambda/4$ plates were used for linearly and circularly polarized experiments, respectively. **(b)** SHG of an $(R\text{-MPEA})_{1.5}PbBr_{3.5}(DMSO)_{0.5}$ nanowire pumped at various wavelengths. **(c)** SHG intensity from the nanowire as function of the rotation angle of the $\lambda/4$ plate. (a–c) Reproduced from Ref. [120]. **(d)** SHG mapping of $(R\text{-ClPEA})_2PbI_4$ microwire. **(e)** Wavelength-dependent SHG of $(R\text{-ClPEA})_2PbI_4$ microwire arrays at the excitation wavelength varying from 720 to 880 nm. **(f)** Linear-polarization-dependent SHG of $(R\text{-ClPEA})_2PbI_4$ microwire arrays. (d–f) Reproduced from Ref. [121]. **(g)** Conceptual illustration of SHG generation of as-prepared microwires. **(h)** Wavelength-dependent SHG intensity of $(S\text{-3AP})_4AgBiBr_{12}$ microwire arrays at wavelengths varying from 760 to 920 nm. **(i)** Polarization-dependent SHG of $(S\text{-3AP})_4AgBiBr_{12}$ microwire arrays. (g–i) Reproduced from Ref. [122].

is not required for THG. It was reported that $(BA)_2(MA)_{n-1}Pb_nI_{3n+1}$ (n = 1–3) nanoflakes displayed strong THG due to the exciton effect enhanced third-order nonlinearity [Figs. 13(a) and (b)]. THG intensity is strongest when the THG emission overlaps with exciton energy and will decrease sharply when THG energy detunes from the exciton peak [124]. In addition, the THG intensity depends on the thickness of 2D perovskite, in which the THG intensity decreases quickly with increased thickness owing to the self-absorption and phase mismatch. Also, perovskites with different n value were mechanically exfoliated for THG measurement [125]. The maximum conversion efficiency is 0.006% for n = 2 perovskite and it is estimated that the $(BA)_2MAPb_2I_7$ (n = 2) nanoflakes have the maximum effective third-order susceptibility $\chi^{(3)}$ of 1.12×10^{-17} $m^2 \cdot V^{-2}$ [Figs. 13(c) and (d)]. The third-order susceptibility $\chi^{(3)}$ decreases with the increased inorganic layer thickness.Strong THG emission was also observed in $(BA)_2MA_{n-1}Pb_nI_{3n+1}$ (n = 1–4) by Jang *et al.* [125]. Due to the

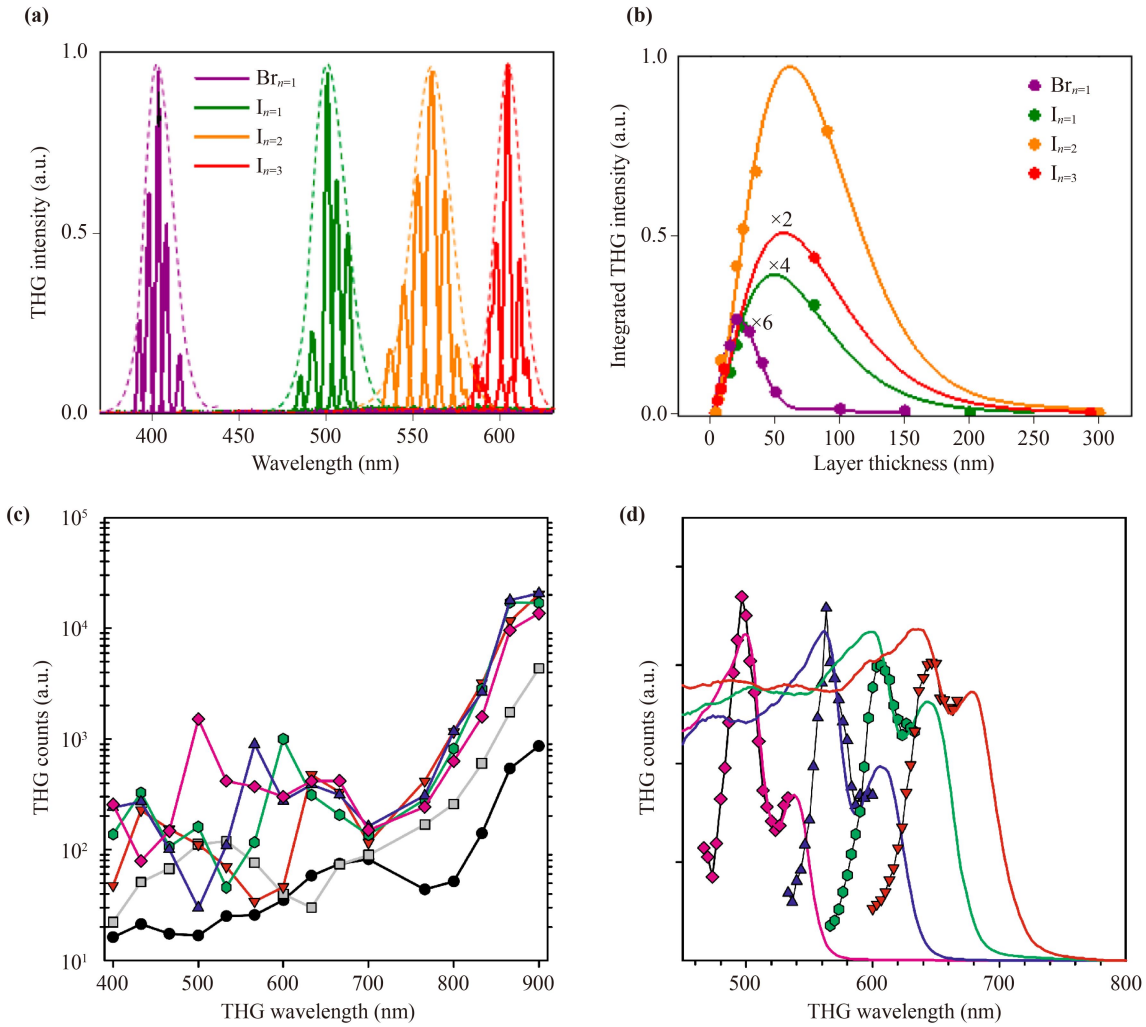

Fig. 13 **(a)** Fundamental wavelength dependence THG of $(BA)_2Pb(I/Br)_4$ and $(BA)_2(MA)_{n-1}Pb_nI_{3n+1}$ (n = 2, 3) perovskite crystals. **(b)** Thickness dependence THG with four different types of crystals excited at resonance. (a, b) Reproduced from Ref. [124]. **(c)** Comparison of THG of $(BA)_2(MA)_{n-1}Pb_nI_{3n+1}$ perovskite, $n = 1$ (purple), $n = 2$ (blue), $n = 3$ (green), $n = 4$ (red), $n = \infty$ and $AgGaSe_2$ (black). **(d)** Fine-scale THG scanned across the band edges of the 2D perovskites, overlaid with the measured absorption spectra (colored traces). (c, d) Reproduced from Ref. [125].

strong quantum confinement effects, the 2D perovskites exhibit 4 times stronger THG at mid-infrared than 3D perovskite $MAPbI_3$.

He *et al.* [126] reported the in-plane anisotropic THG properties of $(C_6H_5(CH_2)_2NH_3)_2PbI_4$ (PEPI), $(C_6H_{11}NH_3)_2PbI_4$ (C_6H_{11}) and $(C_4H_9NH_3)_2PbI_4$ (C4PI) bulk crystal. Though they showed a similar anisotropy of the nonparametric NLO response such as two-photon photoluminescence (2PPL) and there-photon photoluminescence (3PPL) due to the similar lead halide networks of $[PbI_6]^{4-}$ octahedra, PEPI, C_6H_{11} and C_4PI have different THG anisotropic rations of 22.3, 35.7 and 20.4 respectively. This suggests that the anisotropy of THG signals is strongly dependent on the specific crystal structure of the individual flakes.

3.3 Two-photon absorption

TPA comes from third-order nonlinearity and it is a nonparametric process. The TPA properties of $(PEA)_2PbI_4$ perovskite flake was systematically studied by Xiong's group [127]. Under the pump of 800 nm femtosecond pulse laser, the perovskite exhibited a giant TPA coefficient of 211.5 cm·MW^{-1}, which is one order of magnitude larger than other 3D perovskites [Fig. 14(a)]. This giant TPA coefficient is attributed to the enhanced quantum and dielectric confinement effects in multi-quantum-well structure of 2D perovskites. In addition, the TPA coefficient significantly decrease with increased thickness of perovskites flakes [Fig. 14(b)]. Similarly, $(BA)_2(FA)Pb_2Br_7$ ($n = 2$) was synthesized by Luo *et al.* [128] and a TPA coefficient of 5.76 × 10^3 cm·GW^{-1} was obtained under 800 nm fs laser excitation [Fig. 14(c)],

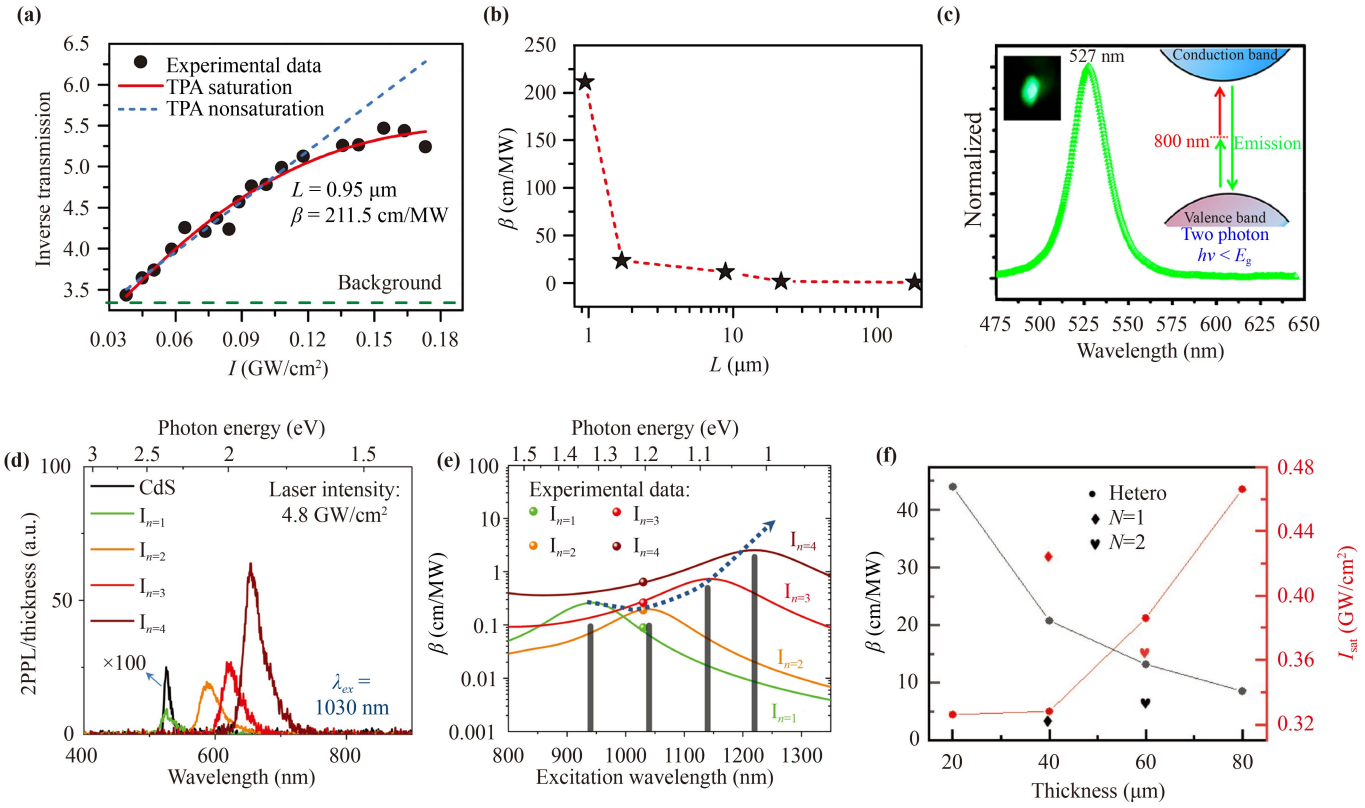

Fig. 14 **(a)** Inverse transmission as a function of peak intensity for $(PEA)_2PbI_4$ flake, fitted by TPA saturation (red curve) and nonsaturation (blue dashed line) models. **(b)** Plot of TPA coefficient versus sample thickness for $(PEA)_2PbI_4$ flakes. (a, b) Reproduced from Ref. [127]. **(c)** PL of $(BA)_2(FA)Pb_2Br_7$ under the excitation at 800 nm [128]. **(d)** 2PPL spectra measured on the 316 nm thick ($I_{n=1}$), 582 nm thick ($I_{n=2}$), 154 nm thick ($I_{n=3}$), 155 nm thick ($I_{n=4}$) and 0.5 mm thick bulk CdS. The 2PPL peaks are normalized by their thickness. **(e)** Experimentally measured (colored dots) and theoretically calculated (colored curves) degenerate TPA spectra. (d, e) Reproduced from Ref. [129]. **(f)** Thickness-dependent TPA coefficient and TPA saturation intensity for $n = 1/n = 2$ heterostructures [130].

which was the first example of achieving prominent TPA in hybrid perovskite ferroelectrics. In addition, $(BA)_2(MA)_{n-1}Pb_nI_{3n+1}$ (n = 1–4) 2D perovskite nanosheets were synthesized for nonlinear optics, exhibiting large TPA coefficient of 0.2–0.64 cm·MW^{-1} under 1030 nm femtosecond pulse laser excitation [Figs. 14(d) and (e)]. As same as SHG and THG, TPA can be also enhanced when the excitation is overlapping with the exciton energy. As an un-conversion process, TPA enables the photodetection of near-infrared light. For instance, the photodetector based on $(BA)_2(MA)_3Pb_4I_{13}$ perovskite nanosheets show excellent near-infrared light absorption with the two-photon-generated current responsivity up to 1.2×10^4 cm^2·W^{-2}·s^{-1} under 1030 nm femtosecond laser pulses excitation [129].

The perovskite heterostructure $(BA)_2PbI_4/(BA)_2(MA)$-Pb_2I_7 was synthesized by our group with strong third-order nonlinearity [130]. A large TPA coefficient of 44 cm·MW^{-1} could be observed in a 20 μm thickness heterostructure and it was accompanied with the multi-photon-induced photoluminescence [Fig. 14(f)]. Similar with previous reports, the TPA coefficient decreases with increased heterostructure thickness due to the nonradiative energy transfer within the heterostructure. The photodetector based on the heterostructure offer ability of dual-band infrared light detection with responsivity of 10^{-7} A·W^{-1}.

In addition, there are many strategies to further exploit the potential of 2PA in 2D perovskites, SiO_2 microsphere was used as hybrid dielectric structure covered on a 2D perovskite flake to enhance TPA emission [131]. Under 800 nm femtosecond pulse laser excitation, the TPA emission with two orders of magnitude higher of could be obtained in the hybrid dielectric structure. In addition, the internal quantum efficiency of 2D perovskite is also improved due to low nonradiative rate.

3.4 Excitonic effect on NLO

The exciton effect also occurs in nonlinear optical process in which the nonlinearity can be enhanced dramatically when the exciton states are related with the intermediate or final state for nonlinear transitions [115]. Stronger resonant enhancement will emerge when

more oscillators are concentrated on the energy states.

The excitonic effect in nonlinear process was discussed by Ito's group in 1991 [132]. $(C_{10}H_{21}NH_3)_2PbI_4$ perovskite crystal show the largest nonlinear optical susceptibility $\chi^{(3)}$ (7×10^{-10} esu) at 1530 nm excitation because the three-photon absorption is inreasonance with the exciton oscillation. Loh *et al.* [124] further studied the THG excitonic resonances of 2D perovskite ($n = 1$–3) and the 2D perovskite exhibits the strongest THG emission at excitonic band gap of 2D perovskite [Fig. 13(a)]. Recently, Jang *et al.* [125] also exploreed the THG of 2D perovskite $BA_2(MA)_{n-1}Pb_nI_{3n+1}$ ($n = 1$–4), and the strong quantum confinement of 2D lead to a four times stronger THG at mid-infrared than 3D perovskite. The variation of THG intensity under different excitation wavelength is consistent with the absorption spectra across the band edges of the 2D perovskites [Fig. 13(d)]. The THG signal is strongly enhanced when the excitation laser energy is in resonance with the exciton absorption energy of 2D perovskite. In addition, this excitonic effect increase with the exciton binding energy caused by the strong confinement effect in 2D perovskite.

The excitonic effect was also observed in TPA process. Ji's group [129] explores the excitonic effect of TPA in 2D perovskite ($n = 1$–4) experimentally and theoretically. Under the 1030 nm femtosecond laser pulse excitation, the $n = 4$ perovskite shows a larger TPA coefficient of 2.5 cm·MW^{-1} than other perovskite ($n = 1$–3) due to the stronger resonance effect. The theoretical model was proposed, which agrees with the experiment results [Fig. 14(e)].

4 Conclusion and outlook

Thanks to the ambient stability, strong quantum confinement effect, large exciton binding energy, 2D perovskites are promising in optoelectronics. It is critical to explore the optical properties to optimize the performance of devices. Herein, we summarized the recent research progress on the optical properties of 2D perovskites. Large exciton binding energy is one of the most important features of 2D perovskites, which makes it possible to achieve efficient light emission at room temperature. In addition to the free exciton, self-trapped excitons originated from strong electron–phonon coupling are also useful in broadband emission. One of the most appealing properties of 2D perovskites is that their optical properties can be engineered via various strategies such as changing inorganic thickness and inorganic/organic components. Specifically, the incorporation of chiral organic molecules can induce chiroptical activities and this kind of chiral responses have intriguing potential in CPL emission, detection and spintronics. Furthermore, 2D perovskites can be integrated with other 2D layered materials to form heterostructures to broaden their functionalities. This article also discussed the nonlinear optical properties of 2D perovskites, which is of great importance in frequency conversion and up-conversion emission/detection. Although great progresses have been achieved in past decade years, there still exist some problems that need to be solved towards practical applications.

(i) Synthesis of large-scale, nontoxic and stable 2D perovskites. At present, most studies focus on the lead-based 2D perovskites due to excellent light absorbing and charge transporting properties. However, the lead-based perovskites are harmful to humans and environment. Lead-based perovskites are also unstable to humidity and temperature despite the existence organic layer. Recently, the Sn-based 2D perovskites have been synthesized due to excellent conductive properties and broadband emission in visible to near infrared range. Whereas, the Sn-based 2D perovskites are unstable and easily to be oxidized to form Sn^{4+}. The lead-free double perovskites are widely concerned as the promising candidates due to nontoxicity and stability and much more efforts need to be devoted to develop high performance 2D double perovskites. On the other hand, it is desirable to achieve controllable synthesis of high quality 2D perovskites with $n > 2$. The alternating organic-inorganic layer arrangement of 2D perovskites makes it possible to study the quantum well properties in the bulk materials. Therefore, the controllable synthesis of 2D perovskites with different inorganic thickness is not only significant for the fundamental research, but also important to tune wavelength range of optical response.

(ii) Mechanism of chirality origin and synthesis of high crystalline quality chiral 2D perovskites. Although most of researcher consider the chiral molecular induce structure distortion as the main reason for chirality origin, there are still lacking depth understand about the chirality origin. We think it is the combination of structure distortion and electronic interactions that responsible for the origin of chirality. The relation between chiral distortion of perovskite and optical chirality of chirality of chiral perovskite needs to be further explored. In addition, establishing proper theoretical model may be one of the effective strategy to investigate chiral origin of chiral perovskite. The crystal structure analysis will also be significant to uncover the chiral mechanism. The CPL emission and detection are the core of the 2D chiral perovskites based devices. Currently, circularly polarized light emission based on 2D chiral perovskite is normally achieved at liquid nitrogen temperature with the CPL degree around 20%. In the future, it is necessary to reveal the mechanism of the origin of chirality completely, which is the guidance to design and synthesize 2D chiral perovskites with high-degree CPL emission at room temperature. The detectivity and detection wavelength range of 2D chiral perovskites based photodetector also needs to be optimized further for polarization detection and imaging.

(iii) Develop applications of 2D chiral perovskites in

valleytronics and spintronics. The ability of generation unbalanced spin-polarized carriers is quite important in valleytronics and spintronics. The valley polarization of TMDs can be only resolved under circularly polarized light illumination or receiving spin-polarized carriers from ferromagnetic materials, which constrains their practical applications. The spin injection from 2D chiral perovskites to TMDs can enable the valley polarization under linearly polarized illumination and even under electrical pumping, which is of great importance in constructing valleytronic devices. Furthermore, the 2D chiral perovskites can behave as a spin valve due to the chiral induce spin selectivity (CISS), which may play an important role in spintronics.

(iv) Potential applications in exciton polaritons. The quantum well structure is a unique feature of 2D perovskites, which enable us to explore the quantum effects in the bulk materials. In addition, the large binding energy of 2D perovskites make it promising in exciton polaritons. The 2D perovskites nanoplates can behave like a Fabry–Pérot cavity. Consequently, the exciton polariton can be achieved without additional cavity. Therefore, 2D perovskites are an excellent platform to explore the nonlinearity of exciton polaritons and Bose–Einstein condensation.

In summary, the unique optical properties of 2D perovskite make it become the "hot topics" in perovskites and 2D materials community in recent years. Deeply understanding their optical properties, exploring the methods to regulate the optical properties and uncovering the physical mechanism of 2D perovskites are essential in the practical applications. Although many challenges remain, we believe that the deeper fundamental understanding and high performance 2D perovskite-based devices will appear in the near feature.

Acknowledgements This work was supported by the National Key Research and Development Program of China (Grant No. 2022YFB2803900), the National Natural Science Foundation of China (Grant Nos. 62074064 and 62005091), and the Innovation Fund of WNLO.

References

1. A. Hubley, A. Bensalah-Ledoux, B. Baguenard, S. Guy, B. Abécassis, and B. Mahler, Chiral perovskite nanoplatelets exhibiting circularly polarized luminescence through ligand optimization, *Adv. Opt. Mater.* 10(19), 2200394 (2022)
2. Y. T. Li, L. Han, H. Liu, K. Sun, D. Luo, X. L. Guo, D. L. Yu, and T. L. Ren, Review on organic–inorganic two-dimensional perovskite-based optoelectronic devices, *ACS Appl. Electron. Mater.* 4(2), 547 (2022)
3. S. Q. Luo, J. F. Wang, B. Yang, and Y. B. Yuan, Recent advances in controlling the crystallization of two-dimensional perovskites for optoelectronic device, *Front. Phys.* 14(5), 53401 (2019)
4. L. Mao, C. C. Stoumpos, and M. G. Kanatzidis, Two-dimensional hybrid halide perovskites: Principles and promises, *J. Am. Chem. Soc.* 141(3), 1171 (2019)
5. H. Wang, C. Fang, H. Luo, and D. Li, Recent progress of the optoelectronic properties of 2D Ruddlesden–Popper perovskites, *J. Semicond.* 40(4), 041901 (2019)
6. F. Wang, X. Zou, M. Xu, H. Wang, H. Wang, H. Guo, J. Guo, P. Wang, M. Peng, Z. Wang, Y. Wang, J. Miao, F. Chen, J. Wang, X. Chen, A. Pan, C. Shan, L. Liao, and W. Hu, Recent progress on electrical and optical manipulations of perovskite photodetectors, *Adv. Sci. (Weinh.)* 8(14), 2100569 (2021)
7. J. Xing, F. Yan, Y. Zhao, S. Chen, H. Yu, Q. Zhang, R. Zeng, H. V. Demir, X. Sun, A. Huan, and Q. Xiong, High-efficiency light-emitting diodes of organometal halide perovskite amorphous nanoparticles, *ACS Nano* 10(7), 6623 (2016)
8. Q. Zhang, Q. Shang, R. Su, T. T. H. Do, and Q. Xiong, Halide perovskite semiconductor lasers: Materials, cavity design, and low threshold, *Nano Lett.* 21(5), 1903 (2021)
9. S. T. Ha, X. Liu, Q. Zhang, D. Giovanni, T. C. Sum, and Q. Xiong, Synthesis of organic–inorganic lead halide perovskite nanoplatelets: Towards high-performance perovskite solar cells and optoelectronic devices, *Adv. Opt. Mater.* 2(9), 838 (2014)
10. Y. Zhao, F. Ma, Z. Qu, S. Yu, T. Shen, H. X. Deng, X. Chu, X. Peng, Y. Yuan, X. Zhang, and J. You, Inactive $(PbI_2)_2RbCl$ stabilizes perovskite films for efficient solar cells, *Science* 377(6605), 531 (2022)
11. V. V. M. Goldschmidt, Die gesetze der krystallochemie, *Naturwissenschaften* 14(21), 477 (1926)
12. L. Pedesseau, D. Sapori, B. Traore, R. Robles, H. H. Fang, M. A. Loi, H. Tsai, W. Nie, J. C. Blancon, A. Neukirch, S. Tretiak, A. D. Mohite, C. Katan, J. Even, and M. Kepenekian, Advances and promises of layered halide hybrid perovskite semiconductors, *ACS Nano* 10(11), 9776 (2016)
13. C. Lan, Z. Zhou, R. Wei, and J. C. Ho, Two-dimensional perovskite materials: From synthesis to energy-related applications, *Mater. Today Energy* 11, 61 (2019)
14. Y. Lekina and Z. X. Shen, Excitonic states and structural stability in two-dimensional hybrid organic–inorganic perovskites, *J. Sci. Adv. Mater. Devices* 4(2), 189 (2019)
15. W. Guo, Z. Yang, J. Dang, and M. Wang, Progress and perspective in Dion–Jacobson phase 2D layered perovskite optoelectronic applications, *Nano Energy* 86, 106129 (2021)
16. J. Guo, T. Liu, M. Li, C. Liang, K. Wang, G. Hong, Y. Tang, G. Long, S. F. Yu, T. W. Lee, W. Huang, and G. Xing, Ultrashort laser pulse doubling by metal-halide perovskite multiple quantum wells, *Nat. Commun.* 11(1), 3361 (2020)
17. Y. I. Dolzhenko, T. Inabe, and Y. Maruyama, *In situ* X-ray observation on the intercalation of weak interaction molecules into perovskite-type layered crystals $(C_9H_{19}NH_3)_2PbI_4$ and $(C_{10}H_{21}NH_3)_2CdCl_4$, *Bull. Chem. Soc. Jpn.* 59(2), 563 (1986)
18. S. Chen and G. Shi, Two-dimensional materials for

halide perovskite-based optoelectronic devices, *Adv. Mater.* 29(24), 1605448 (2017)
19. J. Jagielski, S. Kumar, W. Y. Yu, and C. J. Shih, Layer-controlled two-dimensional perovskites: Synthesis and optoelectronics, *J. Mater. Chem. C* 5(23), 5610 (2017)
20. Y. Chen, Y. Sun, J. Peng, J. Tang, K. Zheng, and Z. Liang, 2D Ruddlesden–Popper perovskites for optoelectronics, *Adv. Mater.* 30(2), 1703487 (2018)
21. X. Gao, X. Zhang, W. Yin, H. Wang, Y. Hu, Q. Zhang, Z. Shi, V. L. Colvin, W. W. Yu, and Y. Zhang, Ruddlesden–Popper Perovskites, Synthesis and optical properties for optoelectronic applications, *Adv. Sci. (Weinh.)* 6(22), 1900941 (2019)
22. G. Long, R. Sabatini, M. I. Saidaminov, G. Lakhwani, A. Rasmita, X. Liu, E. H. Sargent, and W. Gao, Chiral-perovskite optoelectronics, *Nat. Rev. Mater.* 5(6), 423 (2020)
23. H. Tsai, W. Nie, J. C. Blancon, C. C. Stoumpos, R. Asadpour, B. Harutyunyan, A. J. Neukirch, R. Verduzco, J. J. Crochet, S. Tretiak, L. Pedesseau, J. Even, M. A. Alam, G. Gupta, J. Lou, P. M. Ajayan, M. J. Bedzyk, M. G. Kanatzidis, and A. D. Mohite, High-efficiency two-dimensional Ruddlesden–Popper perovskite solar cells, *Nature* 536(7616), 312 (2016)
24. C. C. Stoumpos, C. M. M. Soe, H. Tsai, W. Nie, J. C. Blancon, D. H. Cao, F. Liu, B. Traoré, C. Katan, J. Even, A. D. Mohite, and M. G. Kanatzidis, High members of the 2D Ruddlesden–Popper halide perovskites: Synthesis, optical properties, and solar cells of $(CH_3(CH_2)_3NH_3)_2(CH_3NH_3)_4Pb_5I_{16}$, *Chem* 2(3), 427 (2017)
25. H. P. Wang, S. Li, X. Liu, Z. Shi, X. Fang, and J. H. He, Low-dimensional metal halide perovskite photodetectors, *Adv. Mater.* 33(7), 2003309 (2021)
26. Y. Zhang, Y. Ma, Y. Wang, X. Zhang, C. Zuo, L. Shen, and L. Ding, Lead-free perovskite photodetectors: Progress, challenges, and opportunities, *Adv. Mater.* 33(26), 2006691 (2021)
27. G. Xing, B. Wu, X. Wu, M. Li, B. Du, Q. Wei, J. Guo, E. K. Yeow, T. C. Sum, and W. Huang, Transcending the slow bimolecular recombination in lead-halide perovskites for electroluminescence, *Nat. Commun.* 8(1), 14558 (2017)
28. N. Wang, L. Cheng, R. Ge, S. Zhang, Y. Miao, W. Zou, C. Yi, Y. Sun, Y. Cao, R. Yang, Y. Wei, Q. Guo, Y. Ke, M. Yu, Y. Jin, Y. Liu, Q. Ding, D. Di, L. Yang, G. Xing, H. Tian, C. Jin, F. Gao, R. H. Friend, J. Wang, and W. Huang, Perovskite light-emitting diodes based on solution-processed self-organized multiple quantum wells, *Nat. Photonics* 10(11), 699 (2016)
29. J. Zhou, Y. Chu, and J. Huang, Photodetectors based on two-dimensional layer-structured hybrid lead iodide perovskite semiconductors, *ACS Appl. Mater. Interfaces* 8(39), 25660 (2016)
30. C. C. Stoumpos, D. H. Cao, D. J. Clark, J. Young, J. M. Rondinelli, J. I. Jang, J. T. Hupp, and M. G. Kanatzidis, Ruddlesden–Popper hybrid lead iodide perovskite 2D homologous semiconductors, *Chem. Mater.* 28(8), 2852 (2016)
31. S. Yang, W. Niu, A. L. Wang, Z. Fan, B. Chen, C. Tan, Q. Lu, and H. Zhang, Ultrathin two-dimensional organic–inorganic hybrid perovskite nanosheets with bright, tunable photoluminescence and high stability, *Angew. Chem. Int. Ed.* 56(15), 4252 (2017)
32. W. Paritmongkol, N. S. Dahod, A. Stollmann, N. Mao, C. Settens, S. L. Zheng, and W. A. Tisdale, Synthetic variation and structural trends in layered two-dimensional alkylammonium lead halide perovskites, *Chem. Mater.* 31(15), 5592 (2019)
33. L. Ma, M. G. Ju, J. Dai, and X. C. Zeng, Tin and germanium based two-dimensional Ruddlesden–Popper hybrid perovskites for potential lead-free photovoltaic and photoelectronic applications, *Nanoscale* 10(24), 11314 (2018)
34. X. Li, J. M. Hoffman, and M. G. Kanatzidis, The 2D halide perovskite rulebook: How the spacer influences everything from the structure to optoelectronic device efficiency, *Chem. Rev.* 142, 2230 (2021)
35. J. C. Blancon, A. V. Stier, H. Tsai, W. Nie, C. C. Stoumpos, B. Traore, L. Pedesseau, M. Kepenekian, F. Katsutani, G. T. Noe, J. Kono, S. Tretiak, S. A. Crooker, C. Katan, M. G. Kanatzidis, J. J. Crochet, J. Even, and A. D. Mohite, Scaling law for excitons in 2D perovskite quantum wells, *Nat. Commun.* 9(1), 2254 (2018)
36. T. T. H. Do, A. Granados Del Aguila, D. Zhang, J. Xing, S. Liu, M. A. Prosnikov, W. Gao, K. Chang, P. C. M. Christianen, and Q. Xiong, Bright exciton fine-structure in two-dimensional lead halide perovskites, *Nano Lett.* 20(7), 5141 (2020)
37. H. Mathieu, P. Lefebvre, and P. Christol, Simple analytical method for calculating exciton binding energies in semiconductor quantum wells, *Phys. Rev. B* 46(7), 4092 (1992)
38. T. Ishihara, J. Takahashi, and T. Goto, Optical properties due to electronic transitions in two-dimensional semiconductors $(C_nH_{2n+1}NH_3)_2PbI_4$, *Phys. Rev. B* 42(17), 11099 (1990)
39. X. Li, J. Hoffman, W. Ke, M. Chen, H. Tsai, W. Nie, A. D. Mohite, M. Kepenekian, C. Katan, J. Even, M. R. Wasielewski, C. C. Stoumpos, and M. G. Kanatzidis, Two-dimensional halide perovskites incorporating straight chain symmetric diammonium ions, $(NH_3C_mH_{2m}NH_3)(CH_3NH_3)_{n-1}Pb_nI_{3n+1}$ (m = 4–9; n = 1–4), *J. Am. Chem. Soc.* 140(38), 12226 (2018)
40. S. T. Ha, R. Su, J. Xing, Q. Zhang, and Q. Xiong, Metal halide perovskite nanomaterials: Synthesis and applications, *Chem. Sci. (Camb.)* 8(4), 2522 (2017)
41. Y. Gao, E. Shi, S. Deng, S. B. Shiring, J. M. Snaider, C. Liang, B. Yuan, R. Song, S. M. Janke, A. Liebman-Pelaez, P. Yoo, M. Zeller, B. W. Boudouris, P. Liao, C. Zhu, V. Blum, Y. Yu, B. M. Savoie, L. Huang, and L. Dou, Molecular engineering of organic–inorganic hybrid perovskites quantum wells, *Nat. Chem.* 11(12), 1151 (2019)
42. J. Li, H. Wang, and D. Li, Self-trapped excitons in two-dimensional perovskites, *Front Optoelectron.* 13(3), 225 (2020)
43. D. Cortecchia, S. Neutzner, A. R. Srimath Kandada, E. Mosconi, D. Meggiolaro, F. De Angelis, C. Soci, and A. Petrozza, Broadband emission in two-dimensional

hybrid perovskites: The role of structural deformation, *J. Am. Chem. Soc.* 139(1), 39 (2017)
44. D. Cortecchia, J. Yin, A. Petrozza, and C. Soci, White light emission in low-dimensional perovskites, *J. Mater. Chem. C* 7(17), 4956 (2019)
45. X. Wu, M. T. Trinh, D. Niesner, H. Zhu, Z. Norman, J. S. Owen, O. Yaffe, B. J. Kudisch, and X. Y. Zhu, Trap states in lead iodide perovskites, *J. Am. Chem. Soc.* 137(5), 2089 (2015)
46. R. T. Williams and K. S. Song, The self-trapped exciton, *J. Phys. Chem. Solids* 51(7), 679 (1990)
47. L. Mao, Y. Wu, C. C. Stoumpos, M. R. Wasielewski, and M. G. Kanatzidis, White-light emission and structural distortion in new corrugated two-dimensional lead bromide perovskites, *J. Am. Chem. Soc.* 139(14), 5210 (2017)
48. L. Mao, Y. Wu, C. C. Stoumpos, B. Traore, C. Katan, J. Even, M. R. Wasielewski, and M. G. Kanatzidis, Tunable white-light emission in single-cation-templated three-layered 2D perovskites $(CH_3CH_2NH_3)_4Pb_3Br_{10-x}Cl_x$, *J. Am. Chem. Soc.* 139(34), 11956 (2017)
49. Y. Fang, L. Zhang, L. Wu, J. Yan, Y. Lin, K. Wang, W. L. Mao, and B. Zou, Pressure-induced emission (PIE) and phase transition of a two-dimensional halide double perovskite $(BA)_4AgBiBr_8$ (BA = $CH_3(CH_2)_3NH_3^+$), *Angew. Chem. Int. Ed.* 58(43), 15249 (2019)
50. M. Babaei, V. Ahmadi, and G. Darvish, First-principles study of lead-free Ge-based 2D Ruddlesden–Popper hybrid perovskites for solar cell applications, *Phys. Chem. Chem. Phys.* 24(35), 21052 (2022)
51. K. Tanaka and T. Kondo, Bandgap and exciton binding energies in lead-iodide-based natural quantum-well crystals, *Sci. Technol. Adv. Mater.* 4(6), 599 (2004)
52. P. Cheng, T. Wu, J. Liu, W. Q. Deng, and K. Han, Lead-free, two-dimensional mixed germanium and tin perovskites, *J. Phys. Chem. Lett.* 9(10), 2518 (2018)
53. F. Evers, A. Aharony, N. Bar-Gill, O. Entin-Wohlman, P. Hedeg, O. Hod, P. Jelinek, G. Kamieniarz, M. Lemeshko, K. Michaeli, V. Mujica, R. Naaman, Y. Paltiel, S. Refaely-Abramson, O. Tal, J. Thijssen, M. Thoss, J. M. V. Ruitenbeek, L. Venkataraman, D. H. Waldeck, B. Yan, and L. Kronik, Theory of chirality induced spin selectivity: Progress and challenges, *Adv. Mater.* 34(13), 2106629 (2022)
54. J. Yu, J. Kong, W. Hao, X. Guo, H. He, W. R. Leow, Z. Liu, P. Cai, G. Qian, S. Li, X. Chen, and X. Chen, Broadband extrinsic self-trapped exciton emission in Sn-doped 2D lead-halide perovskites, *Adv. Mater.* 31, e1806385 (2019)
55. J. L. Knutson, J. D. Martin, and D. B. Mitzi, Tuning the band gap in hybrid tin iodide perovskite semiconductors using structural templating, *Inorg. Chem.* 44(13), 4699 (2005)
56. F. Zhang, D. H. Kim, H. Lu, J. S. Park, B. W. Larson, J. Hu, L. Gao, C. Xiao, O. G. Reid, X. Chen, Q. Zhao, P. F. Ndione, J. J. Berry, W. You, A. Walsh, M. C. Beard, and K. Zhu, Enhanced charge transport in 2D perovskites via fluorination of organic cation, *J. Am. Chem. Soc.* 141(14), 5972 (2019)
57. X. Hong, T. Ishihara, and A. V. Nurmikko, Dielectric confinement effect on excitons in PbI_4-based layered semiconductors, *Phys. Rev. B* 45(12), 6961 (1992)
58. L. Mao, W. Ke, L. Pedesseau, Y. Wu, C. Katan, J. Even, M. R. Wasielewski, C. C. Stoumpos, and M. G. Kanatzidis, Hybrid Dion–Jacobson 2D lead iodide perovskites, *J. Am. Chem. Soc.* 140(10), 3775 (2018)
59. S. Silver, S. Xun, H. Li, J. L. Brédas, and A. Kahn, Structural and electronic impact of an asymmetric organic ligand in diammonium lead iodide perovskites, *Adv. Energy Mater.* 10(14), 1903900 (2020)
60. M. P. Hautzinger, D. Pan, A. K. Pigg, Y. Fu, D. J. Morrow, M. Leng, M. Y. Kuo, N. Spitha, D. P. II Lafayette, D. D. Kohler, J. C. Wright, and S. Jin, Band edge tuning of two-dimensional Ruddlesden–Popper perovskites by a cation size revealed through nanoplates, *ACS Energy Lett.* 5(5), 1430 (2020)
61. J. Yan, W. Fu, X. Zhang, J. Chen, W. Yang, W. Qiu, G. Wu, F. Liu, P. Heremans, and H. Chen, Highly oriented two-dimensional formamidinium lead iodide perovskites with a small bandgap of 1.51 eV, *Mater. Chem. Front.* 2(1), 121 (2018)
62. X. Wang, Y. Wang, W. Gao, L. Song, C. Ran, Y. Chen, and W. Huang, Polarization-sensitive halide perovskites for polarized luminescence and detection: Recent advances and perspectives, *Adv. Mater.* 33(12), 2003615 (2021)
63. C. Zhang, X. Wang, and L. Qiu, Circularly polarized photodetectors based on chiral materials: A review, *Front. Chem.* 9, 711488 (2021)
64. Y. Dang, X. Liu, B. Cao, and X. Tao, Chiral halide perovskite crystals for optoelectronic applications, *Matter* 4(3), 794 (2021)
65. Y. Dong, Y. Zhang, X. Li, Y. Feng, H. Zhang, and J. Xu, Chiral perovskites: Promising materials toward next-generation optoelectronics, *Small* 15(39), 1902237 (2019)
66. S. Ma, J. Ahn, and J. Moon, Chiral perovskites for next-generation photonics: From chirality transfer to chiroptical activity, *Adv. Mater.* 33(47), 2005760 (2021)
67. S. Alwan and Y. Dubi, Spinterface origin for the chirality-induced spin-selectivity effect, *J. Am. Chem. Soc.* 143(35), 14235 (2021)
68. H. Lu, C. Xiao, R. Song, T. Li, A. E. Maughan, A. Levin, R. Brunecky, J. J. Berry, D. B. Mitzi, V. Blum, and M. C. Beard, Highly distorted chiral two-dimensional tin iodide perovskites for spin polarized charge transport, *J. Am. Chem. Soc.* 142(30), 13030 (2020)
69. T. Feng, Z. Wang, Z. Zhang, J. Xue, and H. Lu, Spin selectivity in chiral metal-halide semiconductors, *Nanoscale* 13(45), 18925 (2021)
70. G. Long, C. Jiang, R. Sabatini, Z. Yang, M. Wei, L. N. Quan, Q. Liang, A. Rasmita, M. Askerka, G. Walters, X. Gong, J. Xing, X. Wen, R. Quintero-Bermudez, H. Yuan, G. Xing, X. R. Wang, D. Song, O. Voznyy, M. Zhang, S. Hoogland, W. Gao, Q. Xiong, and E. H. Sargent, Spin control in reduced-dimensional chiral perovskites, *Nat. Photonics* 12(9), 528 (2018)
71. J. Ahn, E. Lee, J. Tan, W. Yang, B. Kim, and J. Moon, A new class of chiral semiconductors: Chiral-organic-molecule-incorporating organic–inorganic hybrid perovskites, *Mater. Horiz.* 4(5), 851 (2017)

72. L. Yan, M. K. Jana, P. C. Sercel, D. B. Mitzi, and W. You, Alkyl–aryl cation mixing in chiral 2D perovskites, *J. Am. Chem. Soc.* 143(43), 18114 (2021)
73. J. Ahn, S. Ma, J. Y. Kim, J. Kyhm, W. Yang, J. A. Lim, N. A. Kotov, and J. Moon, Chiral 2D organic inorganic hybrid perovskite with circular dichroism tunable over wide wavelength range, *J. Am. Chem. Soc.* 142(9), 4206 (2020)
74. D. G. Billing and A. Lemmerer, Bis[S-β-phenethylammonium] tribromoplumbate(II), *Acta Crystallogr. Sect. E* 59(6), m381 (2003)
75. D. G. Billing and A. Lemmerer, Synthesis and crystal structures of inorganic–organic hybrids incorporating an aromatic amine with a chiral functional group, *CrystEngComm* 8(9), 686 (2006)
76. L. Wang, Y. Xue, M. Cui, Y. Huang, H. Xu, C. Qin, J. Yang, H. Dai, and M. Yuan, A chiral reduced-dimension perovskite for an efficient flexible circularly polarized light photodetector, *Angew. Chem. Int. Ed.* 59(16), 6442 (2020)
77. J. T. Lin, D. G. Chen, L. S. Yang, T. C. Lin, Y. H. Liu, Y. C. Chao, P. T. Chou, and C. W. Chiu, Tuning the circular dichroism and circular polarized luminescence intensities of chiral 2D hybrid organic–inorganic perovskites through halogenation of the organic ions, *Angew. Chem. Int. Ed.* 60(39), 21434 (2021)
78. Y. Dang, X. Liu, Y. Sun, J. Song, W. Hu, and X. Tao, Bulk chiral halide perovskite single crystals for active circular dichroism and circularly polarized luminescence, *J. Phys. Chem. Lett.* 11(5), 1689 (2020)
79. Z. Guo, J. Li, J. Liang, C. Wang, X. Zhu, and T. He, Regulating optical activity and anisotropic second-harmonic generation in zero-dimensional hybrid copper halides, *Nano Lett.* 22(2), 846 (2022)
80. L. Yao, Z. Zeng, C. Cai, P. Xu, H. Gu, L. Gao, J. Han, X. Zhang, X. Wang, X. Wang, A. Pan, J. Wang, W. Liang, S. Liu, C. Chen, and J. Tang, Strong second- and third-harmonic generation in 1D chiral hybrid bismuth halides, *J. Am. Chem. Soc.* 143(39), 16095 (2021)
81. T. H. Moon, S. J. Oh, and K. M. Ok, $[(R\text{-}C_8H_{12}N)_4][Bi_2Br_{10}]$ and $[(S\text{-}C_8H_{12}N)_4][Bi_2Br_{10}]$: Chiral hybrid bismuth bromides templated by chiral organic cations, *ACS Omega* 3(12), 17895 (2018)
82. F. Ge, B. H. Li, P. Cheng, G. Li, Z. Ren, J. Xu, and X. H. Bu, Chiral hybrid copper(I) halides for high efficiency second harmonic generation with a broadband transparency window, *Angew. Chem. Int. Ed.* 61(10), e202115024 (2022)
83. J. Ma, C. Fang, C. Chen, L. Jin, J. Wang, S. Wang, J. Tang, and D. Li, Chiral 2D perovskites with a high degree of circularly polarized photoluminescence, *ACS Nano* 13(3), 3659 (2019)
84. J. Wang, C. Fang, J. Ma, S. Wang, L. Jin, W. Li, and D. Li, Aqueous synthesis of low-dimensional lead halide perovskites for room-temperature circularly polarized light emission and detection, *ACS Nano* 13(8), 9473 (2019)
85. Y. H. Kim, Y. Zhai, H. Lu, X. Pan, C. Xiao, E. A. Gaulding, S. P. Harvey, J. J. Berry, Z. V. Vardeny, J. M. Luther, and M. C. Beard, Chiral-induced spin selectivity enables a room-temperature spin light-emitting diode, *Science* 371(6534), 1129 (2021)
86. A. Ishii and T. Miyasaka, Direct detection of circular polarized light in helical 1D perovskite-based photodiode, *Sci. Adv.* 6(46), eabd3274 (2020)
87. C. Ye, J. Jiang, S. Zou, W. Mi, and Y. Xiao, Core-shell three-dimensional perovskite nanocrystals with chiral-induced spin selectivity for room-temperature spin light-emitting diodes, *J. Am. Chem. Soc.* 144(22), 9707 (2022)
88. J. Ma, H. Wang, and D. Li, Recent progress of chiral perovskites: Materials, synthesis, and properties, *Adv. Mater.* 33(26), 2008785 (2021)
89. T. He, J. Li, X. Li, C. Ren, Y. Luo, F. Zhao, R. Chen, X. Lin, and J. Zhang, Spectroscopic studies of chiral perovskite nanocrystals, *Appl. Phys. Lett.* 111(15), 151102 (2017)
90. Z. N. Georgieva, Z. Zhang, P. Zhang, B. P. Bloom, D. N. Beratan, and D. H. Waldeck, Ligand coverage and exciton delocalization control chiral imprinting in perovskite nanoplatelets, *J. Phys. Chem. C* 126(37), 15986 (2022)
91. C. T. Wang, K. Chen, P. Xu, F. Yeung, H. S. Kwok, and G. Li, Fully chiral light emission from $CsPbX_3$ perovskite nanocrystals enabled by cholesteric superstructure stacks, *Adv. Funct. Mater.* 29(35), 1903155 (2019)
92. M. K. Jana, R. Song, H. Liu, D. R. Khanal, S. M. Janke, R. Zhao, C. Liu, Z. Valy Vardeny, V. Blum, and D. B. Mitzi, Organic-to-inorganic structural chirality transfer in a 2D hybrid perovskite and impact on Rashba–Dresselhaus spin–orbit coupling, *Nat. Commun.* 11(1), 4699 (2020)
93. Y. H. Kim, R. Song, J. Hao, Y. Zhai, L. Yan, T. Moot, A. F. Palmstrom, R. Brunecky, W. You, J. J. Berry, J. L. Blackburn, M. C. Beard, V. Blum, and J. M. Luther, The structural origin of chiroptical properties in perovskite nanocrystals with chiral organic ligands, *Adv. Funct. Mater.* 32(25), 2200454 (2022)
94. Z. N. Georgieva, B. P. Bloom, S. Ghosh, and D. H. Waldeck, Imprinting chirality onto the electronic states of colloidal perovskite nanoplatelets, *Adv. Mater.* 30(23), 1800097 (2018)
95. J. Zhang, X. Zhu, M. Wang, and B. Hu, Establishing charge-transfer excitons in 2D perovskite heterostructures, *Nat. Commun.* 11(1), 2618 (2020)
96. J. Wang, J. Li, S. Lan, C. Fang, H. Shen, Q. Xiong, and D. Li, Controllable growth of centimeter-sized 2D perovskite heterostructures for highly narrow dual-band photodetectors, *ACS Nano* 13(5), 5473 (2019)
97. Y. Fu, W. Zheng, X. Wang, M. P. Hautzinger, D. Pan, L. Dang, J. C. Wright, A. Pan, and S. Jin, Multicolor heterostructures of two-dimensional layered halide perovskites that show interlayer energy transfer, *J. Am. Chem. Soc.* 140(46), 15675 (2018)
98. E. Shi, B. Yuan, S. B. Shiring, Y. Gao, Y. Akriti, Y. Guo, C. Su, M. Lai, P. Yang, J. Kong, B. M. Savoie, Y. Yu, and L. Dou, Two-dimensional halide perovskite lateral epitaxial heterostructures, *Nature* 580(7805), 614 (2020)
99. E. Akriti, E. Shi, S. B. Shiring, J. Yang, C. L. Atencio-

Martinez, B. Yuan, X. Hu, Y. Gao, B. P. Finkenauer, A. J. Pistone, Y. Yu, P. Liao, B. M. Savoie, and L. Dou, Layer-by-layer anionic diffusion in two-dimensional halide perovskite vertical heterostructures, *Nat. Nanotechnol.* 16(5), 584 (2021)

100. Y. Chen, Z. Liu, J. Li, X. Cheng, J. Ma, H. Wang, and D. Li, Robust interlayer coupling in two-dimensional perovskite/monolayer transition metal dichalcogenide heterostructures, *ACS Nano* 14(8), 10258 (2020)
101. Y. Chen, J. Ma, Z. Liu, J. Li, X. Duan, and D. Li, Manipulation of valley pseudospin by selective spin injection in chiral two-dimensional perovskite/monolayer transition metal dichalcogenide heterostructures, *ACS Nano* 14(11), 15154 (2020)
102. E. Shi, Y. Gao, B. P. Finkenauer, A. H. Akriti, A. H. Coffey, and L. Dou, Two-dimensional halide perovskite nanomaterials and heterostructures, *Chem. Soc. Rev.* 47(16), 6046 (2018)
103. F. Fang, Y. Wan, H. Li, S. Fang, F. Huang, B. Zhou, K. Jiang, V. Tung, L. J. Li, and Y. Shi, Two-dimensional $Cs_2AgBiBr_6/WS_2$ heterostructure-based photodetector with boosted detectivity via interfacial engineering, *ACS Nano* 16(3), 3985 (2022)
104. Q. Zhang, E. Linardy, X. Wang, and G. Eda, Excitonic energy transfer in heterostructures of quasi-2D perovskite and monolayer WS_2, *ACS Nano* 14(9), 11482 (2020)
105. W. Yao, D. Yang, Y. Chen, J. Hu, J. Li, and D. Li, Layer-number engineered momentum-indirect interlayer excitons with large spectral tunability, *Nano Lett.* 22(17), 7230 (2022)
106. T. Ye, J. Li, and D. Li, Charge-accumulation effect in transition metal dichalcogenide heterobilayers, *Small* 15(42), 1902424 (2019)
107. A. F. Rigosi, H. M. Hill, Y. Li, A. Chernikov, and T. F. Heinz, Probing interlayer interactions in transition metal dichalcogenide heterostructures by optical spectroscopy: MoS_2/WS_2 and $MoSe_2/WSe_2$, *Nano Lett.* 15(8), 5033 (2015)
108. H. Fang, C. Battaglia, C. Carraro, S. Nemsak, B. Ozdol, J. S. Kang, H. A. Bechtel, S. B. Desai, F. Kronast, A. A. Unal, G. Conti, C. Conlon, G. K. Palsson, M. C. Martin, A. M. Minor, C. S. Fadley, E. Yablonovitch, R. Maboudian, and A. Javey, Strong interlayer coupling in van der Waals heterostructures built from single-layer chalcogenides, *Proc. Natl. Acad. Sci. USA* 111(17), 6198 (2014)
109. P. Rivera, J. R. Schaibley, A. M. Jones, J. S. Ross, S. Wu, G. Aivazian, P. Klement, K. Seyler, G. Clark, N. J. Ghimire, J. Yan, D. G. Mandrus, W. Yao, and X. Xu, Observation of long-lived interlayer excitons in monolayer $MoSe_2$–WSe_2 heterostructures, *Nat. Commun.* 6(1), 6242 (2015)
110. P. K. Nayak, Y. Horbatenko, S. Ahn, G. Kim, J. U. Lee, K. Y. Ma, A. R. Jang, H. Lim, D. Kim, S. Ryu, H. Cheong, N. Park, and H. S. Shin, Probing evolution of twist-angle-dependent interlayer excitons in $MoSe_2$/WSe_2 van der Waals heterostructures, *ACS Nano* 11(4), 4041 (2017)
111. A. Elbanna, K. Chaykun, Y. Lekina, Y. Liu, B. Febriansyah, S. Li, J. Pan, Z. X. Shen, and J. Teng, Perovskite-transition metal dichalcogenides heterostructures: Recent advances and future perspectives, *Opto-Electron. Sci.* 1(8), 220006 (2022)
112. Q. Wei, X. Wen, J. Hu, Y. Chen, Z. Liu, T. Lin, and D. Li, Site-controlled interlayer coupling in WSe_2/2D perovskite heterostructure, *Sci. China Mater.* 65(5), 1337 (2022)
113. G. Zhan, J. Zhang, L. Zhang, Z. Ou, H. Yang, Y. Qian, X. Zhang, Z. Xing, L. Zhang, C. Li, J. Zhong, J. Yuan, Y. Cao, D. Zhou, X. Chen, H. Ma, X. Song, C. Zha, X. Huang, J. Wang, T. Wang, W. Huang, and L. Wang, Stimulating and manipulating robust circularly polarized photoluminescence in achiral hybrid perovskites, *Nano Lett.* 22(10), 3961 (2022)
114. J. Xu, X. Li, J. Xiong, C. Yuan, S. Semin, T. Rasing, and X. H. Bu, Halide perovskites for nonlinear optics, *Adv. Mater.* 32(3), 1806736 (2020)
115. G. Wang, S. Mei, J. Liao, W. Wang, Y. Tang, Q. Zhang, Z. Tang, B. Wu, and G. Xing, Advances of nonlinear photonics in low-dimensional halide perovskites, *Small* 17(43), 2100809 (2021)
116. X. Wen, Z. Gong, and D. Li, Nonlinear optics of two-dimensional transition metal dichalcogenides, *InfoMat* 1(3), 317 (2019)
117. X. Han, Y. Zheng, S. Chai, S. Chen, and J. Xu, 2D organic–inorganic hybrid perovskite materials for nonlinear optics, *Nanophotonics* 9(7), 1787 (2020)
118. Y. Zhou, Y. Huang, X. Xu, Z. Fan, J. B. Khurgin, and Q. Xiong, Nonlinear optical properties of halide perovskites and their applications, *Appl. Phys. Rev.* 7(4), 041313 (2020)
119. T. T. H. Do, A. G. Del Aguila, J. Xing, S. Liu, and Q. Xiong, Direct and indirect exciton transitions in two-dimensional lead halide perovskite semiconductors, *J. Chem. Phys.* 153(6), 064705 (2020)
120. C. Yuan, X. Li, S. Semin, Y. Feng, T. Rasing, and J. Xu, Chiral lead halide perovskite nanowires for second-order nonlinear optics, *Nano Lett.* 18(9), 5411 (2018)
121. J. Zhao, Y. Zhao, Y. Guo, X. Zhan, J. Feng, Y. Geng, M. Yuan, X. Fan, H. Gao, L. Jiang, Y. Yan, and Y. Wu, Layered metal-halide perovskite single-crystalline microwire arrays for anisotropic nonlinear optics, *Adv. Funct. Mater.* 31(48), 2105855 (2021)
122. Z. Yu, S. Cao, Y. Zhao, Y. Guo, M. Dong, Y. Fu, J. Zhao, J. Yang, L. Jiang, and Y. Wu, Chiral lead-free double perovskite single-crystalline microwire arrays for anisotropic second-harmonic generation, *ACS Appl. Mater. Interfaces* 14(34), 39451 (2022)
123. W. J. Wei, X. X. Jiang, L. Y. Dong, W. W. Liu, X. B. Han, Y. Qin, K. Li, W. Li, Z. S. Lin, X. H. Bu, and P. X. Lu, Regulating second-harmonic generation by van der Waals interactions in two-dimensional lead halide perovskite nanosheets, *J. Am. Chem. Soc.* 141(23), 9134 (2019)
124. I. Abdelwahab, G. Grinblat, K. Leng, Y. Li, X. Chi, A. Rusydi, S. A. Maier, and K. P. Loh, Highly enhanced third-harmonic generation in 2D perovskites at excitonic resonances, *ACS Nano* 12(1), 644 (2018)
125. F. O. Saouma, C. C. Stoumpos, J. Wong, M. G. Kanatzidis, and J. I. Jang, Selective enhancement of optical nonlinearity in two-dimensional organic–inor-

ganic lead iodide perovskites, *Nat. Commun.* 8(1), 742 (2017)

126. Z. Chen, Q. Zhang, M. Zhu, H. Chen, X. Wang, S. Xiao, K. P. Loh, G. Eda, J. Meng, and J. He, In-plane anisotropic nonlinear optical properties of two-dimensional organic–inorganic hybrid perovskite, *J. Phys. Chem. Lett.* 12(29), 7010 (2021)
127. W. Liu, J. Xing, J. Zhao, X. Wen, K. Wang, P. Lu, and Q. Xiong, Giant two-photon absorption and its saturation in 2D organic–inorganic perovskite, *Adv. Opt. Mater.* 5(7), 1601045 (2017)
128. L. Li, X. Shang, S. Wang, N. Dong, C. Ji, X. Chen, S. Zhao, J. Wang, Z. Sun, M. Hong, and J. Luo, Bilayered hybrid perovskite ferroelectric with giant two-photon absorption, *J. Am. Chem. Soc.* 140(22), 6806 (2018)
129. F. Zhou, I. Abdelwahab, K. Leng, K. P. Loh, and W. Ji, 2D perovskites with giant excitonic optical nonlinearities for high-performance sub-bandgap photodetection, *Adv. Mater.* 31(48), 1904155 (2019)
130. J. Wang, Y. Mi, X. Gao, J. Li, J. Li, S. Lan, C. Fang, H. Shen, X. Wen, R. Chen, X. Liu, T. He, and D. Li, Giant nonlinear optical response in 2D perovskite heterostructures, *Adv. Opt. Mater.* 7(15), 1900398 (2019)
131. W. Liu, X. Li, Y. Song, C. Zhang, X. Han, H. Long, B. Wang, K. Wang, and P. Lu, Cooperative enhancement of two-photon-absorption-induced photoluminescence from a 2D perovskite-microsphere hybrid dielectric structure, *Adv. Funct. Mater.* 28(26), 1707550 (2018)
132. C. Q. Xu, T. Kondo, H. Sakakura, K. Kumatat, Y. Takahashit, and R. Ito, Optical third-harmonic generation in layered perovskite-type material $(C_{10}H_{21}NH_3)_2$-PbI_4, *Solid State Commun.* 79(3), 245 (1991)